AD-A069 589 BOEING CO SEATTLE WASH F/G 13/5

INVESTIGATION OF PENETRATION OF ELECTROMAGNETIC ENERGY THROUGH --ETC(U)

APR 79 D F STRAWE, L D PISZKER N00019-79-C-0058

UNCLASSIFIED D180-25240-1 NL

1 OF 1

AD A069589

END

DATE FILMED

7-79

DDC

APPROVED FOR PUBLIC RELEASE;
DISTRIBUTION UNLIMITED

LEVEL II

Contract N00019-79-C-0058

B.S.

AD A069589

REPORT D180-25240-1

(6) Investigation of Penetration of Electromagnetic Energy through Joints in Advanced Composite Structures.

INVESTIGATION OF PENETRATION OF ELECTROMAGNETIC ENERGY THROUGH JOINTS IN ADVANCED COMPOSITE STRUCTURES

(10) D.F. Strawe
L.D. Piszker
D.F. Strawe
L.D. Piszker

DDC
RECEIVED
JUN 8 1979
C

THE BOEING COMPANY
P.O. BOX 3707
SEATTLE, WASHINGTON 98124

(11) Apr 79

(14) D180-25240-1

APRIL 1979

INTERIM REPORT

(15) N00019-79-C-0058

(12) 91p

PREPARED FOR
NAVAL AIR SYSTEMS COMMAND
DEPARTMENT OF THE NAVY
ARLINGTON, VIRGINIA 20360

DDC FILE COPY

79 06 05 032

(9) Interim

Contract No. N00019-79-C-0058

APPROVED FOR PUBLIC RELEASE;
DISTRIBUTION UNLIMITED

059 600

TABLE OF CONTENTS

	Page No.
1.0 INTRODUCTION	5
2.0 JOINT AND MATERIAL PARAMETERS	7
2.1 Diffusion	7
2.2 Mesh Aperture Coupling	11
2.3 Joint Coupling	11
2.4 Measurement Concepts	11
2.4.1 Surface Transfer Impedance	13
2.4.2 Surface Transfer Admittance	13
2.4.3 Joint Coupling Admittance	15
3.0 THEORETICAL FORMULATION	18
4.0 MEASUREMENT SCHEMES EVALUATED	24
4.1 The Quadraxial Test Concept	24
4.2 The Stripline Test Concept	31
4.3 The "Flat-Plate Test" Concept	35
4.4 The Anechoic Chamber	41
5.0 CHARACTERISTICS OF EXISTING TEST FACILITIES	47
5.1 Magnetic Shielding Effectiveness Test (Flat Plate Facility)	47
5.1.1 CW Driver	51
5.1.2 Shield Box	51
5.1.3 Monitoring Recording System	52
5.1.4 Test Setup Evaluation	52
5.2 Quadraxial Shielding Test (QUADRAX Facility)	56
5.2.1 Quadraxial Test Facility	56
5.2.2 CW Tests	58
5.3 The Anechoic Chamber	66
6.0 REVIEW OF INSTRUMENTATION SYSTEMS USED TO MEASURE MICROWAVE LEAKAGE THROUGH PANELS	78
6.1 Anechoic Chamber: Preliminary Evaluation	80
6.2 Preliminary Conclusions	81

79 06 05 032

TABLE OF CONTENTS (continued)

	Page No.
7.0 SUMMARY	83
8.0 RECOMMENDATIONS	87
REFERENCES	89

Accession For
NTIS GRA&I ☑
DDC TAB ☐
Unannounced ☐
Justification
By
Distribution/
Availability Codes
Dist | Avail and/or special
A

LIST OF FIGURES

Figure No.	Title	Page No.
1	The Relation Between Surface Response and Internal Fields	8
2	Diffusion	9
3	Quasistatic Aperture Coupling	10
4	Joint Coupling	12
5	Surface Transfer Impedance and Admittance	14
6	Joint Admittance	16
7	Cylindrical Test Concept: Z_T, Y_T, Y_J	17
8	Material Joints	20
9	Quadrax Geometry	25
10	Stripline Facility	32
11	Stripline Concept	33
12	Magnetic Shielding Effectiveness Equations for Flat Plate Test	37
13	Close Conductor Proximity Effect	40
14	The Anechoic Chamber	42
15	H-Field S.E. Test Setup	48
16	H-Field S.E. Test Instrumentation	49
17	Flat Plate S.E. Test Equipment	50
18	Test Sample in Screen Box	53
19	MSE Test System Evaluation Data	54
20	Schematic of Quadraxial Test Fixture	57
21	Sample Cylinder Clamping Arrangement	59
22	Perforated Aluminum Test Sample in Quadrax	60
23	Quadrax - CW Drive and Monitoring Instrumentation	61
24	Typical Quadraxial Test Facility Evaluation Data	64
25	Freespace Transmission Test System	67
26	Anechoic Chamber - Transmitter	68
27	Sample Holder - Disassembled	69

LIST OF FIGURES (continued)

Figure No.	Title	Page No.
28	Four-Ply Transmission Data, 1.0 to 1.7 GHz	71
29	Four-Ply Transmission Data, 1.7 to 2.0 GHz	71
30	Four-Ply Transmission Data, 2.0 to 2.6 GHz	71
31	Four-Ply Transmission Data, 2.6 to 3.0 GHz	71
32	Conductivity Versus Frequency	73
33	Test Specimen Edge Treatment Concept	76
34	Microwave Measurement System	79

1.0 INTRODUCTION

This interim report is submitted by the Engineering Technology Group of the Boeing Aerospace Company to describe the effort accomplished to date on Naval Air Systems Command Contract N00019-79-C-0058. The objectives of this effort are to conduct an investigation of the effects of electromagnetic energy on advanced composite aircraft structures and their associated avionic/electrical equipment. The primary objective of this investigation is to develop test techniques to evaluate the coupling of electromagnetic energy through joints in the composite materials within the frequency range 10 kHz to 18 GHz. A test setup will be designed, fabricated, and checked out to perform measurements over a portion of this frequency range and joint admittance data will be obtained on a variety of structural joint samples. At the conclusion of this investigation, the test fixture will be delivered to NASC.

A substantial body of data has been taken[1] on electrical material and joint parameters in the 0-100 MHz frequency range. Graphite epoxy composites, metal foils and screens, and flame spray coatings, and joints in these have been measured and reported extensively. Reliable means for measuring a wide range of parameter values has been developed, i.e., the "Quadrax" and "FPT" facilities.

The "Quadrax" requires costly cylindrical test samples and requires time consuming sample mounting. The FPT uses convenient flat plate samples but exhibits a much lower sensitivity and "dynamic range" and has not been developed for joint measurement. Both of these schemes are extendable into the lower UHF range but little work has been done along this line. Various other schemes have been used successfully below 100 MHz including the coupled stripline approach.

Above 100 MHz much less work has been done. Much of that is of questionable quality being apparently polluted by leakage around the sample. That involving small samples transverse to coaxial lines and waveguides are questionable due to unusual current distributions of abnormally thin anisotropic samples. Also, data involving closure of a box enclosure with a composite sample suffers from the current distribution problem and is therefore not extendable or usable in other applications of the same material since it cannot (or at least has not been) be reduced to basic material or joint data. The frequency range above 100 MHz needs the most work in view of the lack of data and established measurement techniques, and the sizable RADAR threat environments existing there.

The initial phase of this program is aimed at providing an analytical description and performance data on joint and material data measurement systems so that priorities for measurement facility development can be set. The field of study is limited essentially to the use of rectangular flat plate samples in the 0-18 GHz range. Analysis and data on the Quadrax is presented, however, as a standard of comparison. The Quadrax, FPT, coupled stripline, and anechoic chamber measurement concepts are explored and rated according to usable frequency, sensitivity, accuracy, and ease of measurement.

2.0 JOINT AND MATERIAL PARAMETERS

The general problem of calculating the fields inside of a given shield in terms of the current and charge (normal E-field) on the exterior is complicated, requiring a detailed knowledge of shield shape and local electrical (coupling) properties[1]. The interior fields are represented in Figure 1 as a linear combination of the effects of diffusion, aperture, and joint coupling. TEM coupling and discrete aperture coupling are not basically a function of the shield itself and are not included.

2.1 DIFFUSION

Figure 2 shows the relation between the surface current density on a shield exterior and the tangential electric field produced at the inside surface due to skin diffusion. The proportionality factor between them is the diffusion surface transfer impedance, z_{sd}. The form of z_{sd} for thin foil surfaces, derived by Schelkunoff[2], is given in terms of frequency, material permeability, conductivity, and thickness. The factor z_{sd} can be considered a basic material coupling parameter.

2.2 MESH APERTURE COUPLING

Aperture coupling through meshes can be described macroscopically by collecting the effects of electric and magnetic quasistatic coupling through individual mesh apertures. It is well known that the fields on the "shadow" side of a surface with a small aperture can be determined approximately from equivalent electric and magnetic dipole moments, at the aperture location, which are proportional to the current density (J_s) and normal electric (E_n) field produced on the "illuminated" side with the aperture "short circuited". This is indicated in Figure 3; $\overline{p}$ and $\overline{m}$

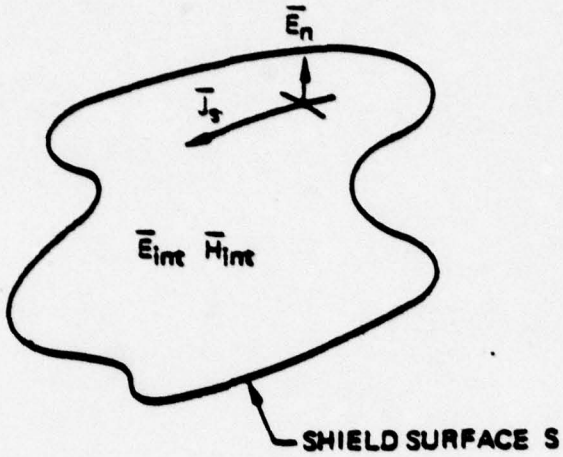

$$\begin{Bmatrix} \bar{E}_{int} \\ \bar{H}_{int} \end{Bmatrix} = \oint\!\!\oint_S \left[(\bar{\bar{G}}_d + \bar{\bar{G}}_m + \bar{\bar{G}}_j) \cdot \bar{J}_s + \bar{\bar{G}}_p \cdot \bar{E}_n \right] ds$$

Skin diffusion:

$\bar{\bar{G}}_d \sim z_{sd}$ (open circuit diffusion transfer impedance: ohms/square)

Distributed aperture coupling (meshes)

$\bar{\bar{G}}_p \sim P$ (surface electric polarizability: farads)

$\bar{\bar{G}}_m \sim M$ (surface magnetic polarizability: meters)

Joint coupling

$\bar{\bar{G}}_j \sim \frac{1}{Y_j}$;

Y_j (joint admittance per unit of joint width or run: mhos/meter)

Figure 1: The Relation Between Surface Response and Internal Fields

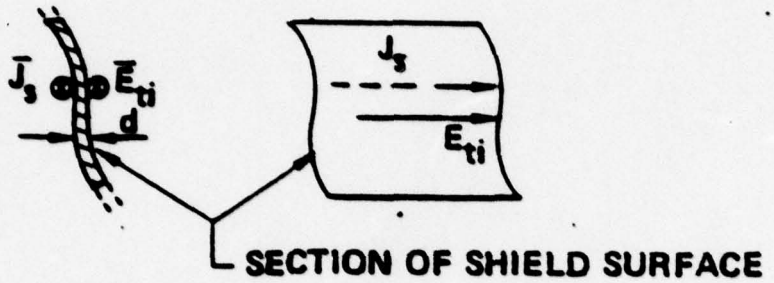

$$\bar{E}_{ti} = z_{sd}\ \bar{J}_s$$

$$z_{sd} = \frac{E_{ti}\ \text{(inner surface tangential electric field)}}{J_s\ \text{(outer surface skin current)}}$$

THIN FOIL SURFACE:

$$z_{sd} = \frac{\hat{\eta}}{\sinh \hat{\gamma} d} \quad ; \ \hat{\eta} = \sqrt{\frac{j\omega\mu}{\sigma}} \quad \& \ \hat{\gamma} = \sqrt{j\omega\mu\sigma}$$

Figure 2: Diffusion

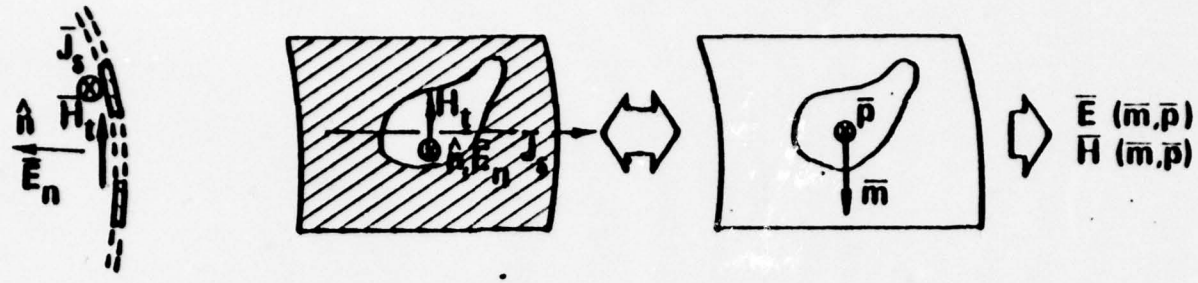

Arrays of small apertures:

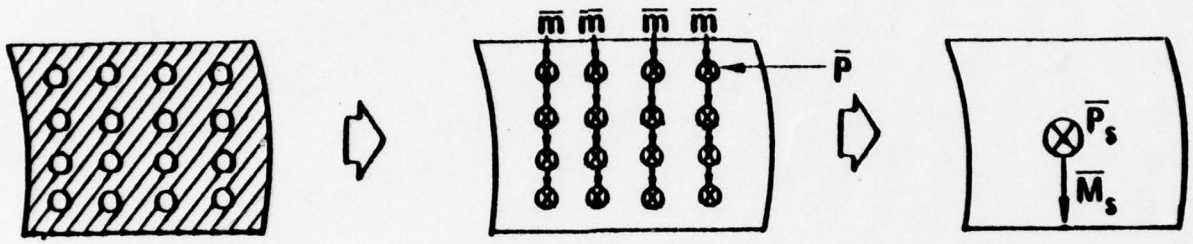

$\bar{P}_s$ (electric dipole moment/unit area) = $P\,\bar{E}_n$

$\bar{M}_s$ (magnetic dipole moment/unit area) = $M\,\hat{n} \times \bar{J}_s$

P (electric surface polarizability) = $n\alpha_E$

M (magnetic surface polarizability) = $n\alpha_H$

Example: For circular apertures of radius r_o

$$\alpha_E = \frac{4\epsilon}{3} r_o^3 \qquad \alpha_H = \frac{8}{3} r_o^3$$

Figure 3: Quasistatic Aperture Coupling

are the equivalent electric and magnetic dipole moments, respectively. $\overline{m}$ is directed parallel to the exterior magnetic field $\overline{H} = \overline{J}_s \times \hat{n}$ and $\overline{p}$ is directed parallel to $\overline{E}_n$. Therefore, an array of apertures, such as the holes in a mesh, can be represented as an array of dipole moments. Since the individual moments cannot be distinguished at distances of the order of a few mesh hole spacings, it is reasonable to collect them into magnetic and electric dipole moments per unit area, $\overline{M}_s$ and $\overline{P}_s$, respectively. The proportionality factors relating $\overline{M}_s$ and $\overline{P}_s$ to $\overline{J}_s$ and $\overline{E}_n$ are, respectively, M (magnetic surface polarizability) and P (electric surface polarizability). M and P are basic material coupling parameters for meshes. They are proportional to the number of apertures per unit area n and to the normalized polarizabilities (α_E and α_H) for the individual apertures (holes). These latter are functions of hole size and orientation, if non-circular, and are generally proportional to linear hole dimension cubed.

2.3 JOINT COUPLING

Well formed joints in shield material (those of uniform construction and good electrical contact and without large cracks or apertures) can be described in terms of a distributed joint transfer admittance per unit of joint width. A section of shield surface containing such a joint is shown in Figure 4. The exterior surface current density J_s flowing across the joint produces a voltage V_j across the joint on the inside. For a linear joint contact impedance the interior joint voltage is proportional to exterior surface current $I_{tot} = J_s W$ and inversely proportional to joint width W. The proportionality factor between V_j and J_s is Y_j, the joint admittance per unit of joint width, i.e., $J_s = Y_j V_j$.

2.4 MEASUREMENT CONCEPTS

A complete set of material surface coupling parameters allowing interior field calculations in a general shielding application is z_{sd}, P,

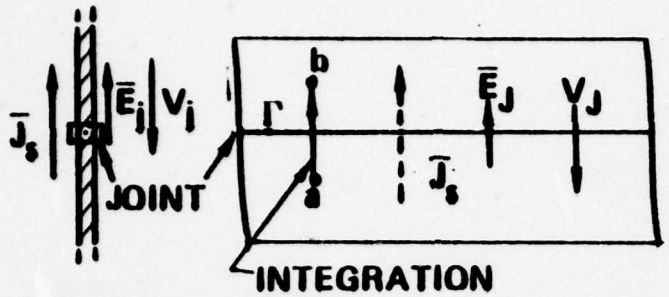

Joint voltage:

$$V_J = \int_{a\,\Gamma}^{b} \bar{E}_J \cdot d\bar{l} = \frac{J_s}{Y_J}$$

Y_J (joint coupling admittance per unit joint width):

$$Y_J = \frac{J_s}{V_J} \quad \text{(mhos/meter)}$$

Example: Perfect sheets with joint

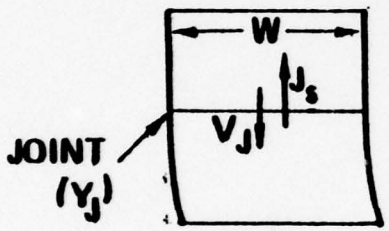

1. **Total joint admittance:**
   $$Y_{tot} = Y_J W$$
2. **Total joint current:**
   $$I_{tot} = J_s W$$
3. **Joint voltage:**
   $$V_J = \frac{I_{tot}}{Y_{tot}} = \frac{J_s W}{Y_J W} = \frac{J_s}{Y_J}$$

Figure 4: Joint Coupling

M, Y_j. At low frequencies, it is convenient to determine these parameters from a series of measurements on electrically small cylindrical samples of material. At higher frequencies, samples will be electrically large and measurement techniques will change. In any case, the cylindrical concepts illustrate the significance of the parameters involved.

2.4.1 Surface Transfer Impedance

If a long cylindrical section of the shielding material is driven externally with a longitudinal, azimuthally uniform surface current density J_s (total current I_s), a uniform longitudinal E-field is produced internally (E_i) (Figure 5a). The proportionality factor between J_s and E_i is the surface transfer impedance, z_s. The factor relating I_s to E_i is Z_T, the cylindrical transfer impedance per unit length. Both diffusion and magnetic aperture coupling are involved in the production of E_i; it can be shown that $z_s = z_{sd} + \frac{j\omega\mu_o M}{2}$. Since z_{sd} and $\frac{j\omega\mu_o M}{2}$ act together as an indistinguishable unit in this test case and in general, there is no need to separate them; only z_s need be determined.

In an electrically short cylindrical sample, the interior field can be determined by installing a coaxial sense rod shorted at one end. The open-circuit voltage at the other end together with the sample length, sample circumference, and the drive current determines z_s.

2.4.2 Surface Transfer Admittance

The electric aperture coupling of mesh shielding materials is described by P. It can be determined by measuring the capacitive coupling through a mesh cylinder between concentric cylinders inside and outside of the mesh (Figure 5b). It can be shown [3,4] that the coupling or transfer capacitance (C_T) is determined by P, the exterior and interior capacitance (C_{ext} and C_{int}), and the mesh sample circumference. P is determined by the

Surface transfer impedance
(diffusion and mag. aperture coupling)

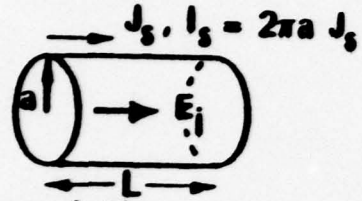

$E_i = J_s\ z_s = I_s\ Z_T$

WHERE

$z_s = z_{sd} + \frac{j\omega\mu_0 M}{2}$ (ohms/square)

$Z_T = \frac{z_s}{2\pi a}$ (ohms/meter)

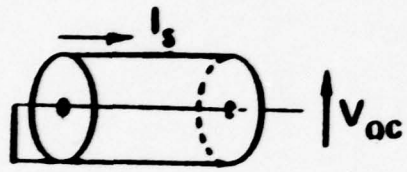

$V_{oc} = Z_T L\ I_s$

(a)

Surface transfer admittance
(electric aperture coupling)

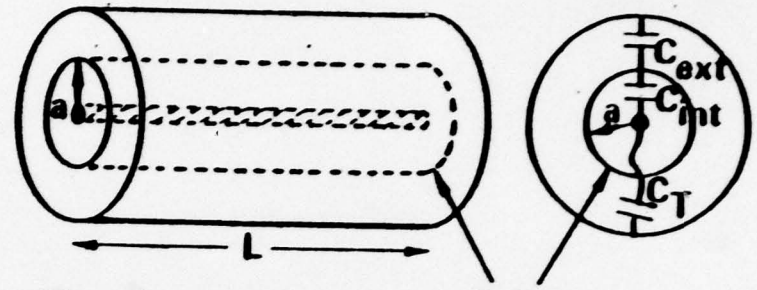

TEST SURFACE

Transfer capacitance:

$$C_T = \frac{P\ C_{int}\ C_{ext}}{4\pi a \epsilon^2} \quad \text{(farads/meter)}$$

Transfer admittance per unit length:

$Y_T = j\omega C_T$

(b)

Figure 5: Surface Transfer Inpedance and Admittance

given formula once the capacitances are measured. The transfer admittance per unit length for the cylinder is $Y_T = j\omega C_T$.

2.4.3 Joint Coupling Admittance

If a joint is formed into a cylindrical sample driven as before with J_s (or I_s) with a coaxial sense rod shorted at one end, the open-circuit sense voltage is related to I_s by $Z_T L + \frac{1}{Y_J C}$ where L and C are the sample length and circumference, respectively (Figure 6). If Z_T is determined from a measurement on an unjointed sample, then Y_J is determined.

The cylindrical test data Z_T, Y_T, Y_J are entirely equivalent to the material properties z_{sd}, P, M, Y_J. The latter set is, of course, applicable to any shape surface and any frequency range.

As a further demonstration of the significance of these parameters a schematic representation of the quadraxial test facility (shown in its triaxial equivalent form for simplicity) is shown in Figure 7. Low frequency equivalent circuits for Z_T, Y_T, and Y_J coupling are also shown, indicating the coupling mechanisms of each.

c) **Joint coupling admittance:**

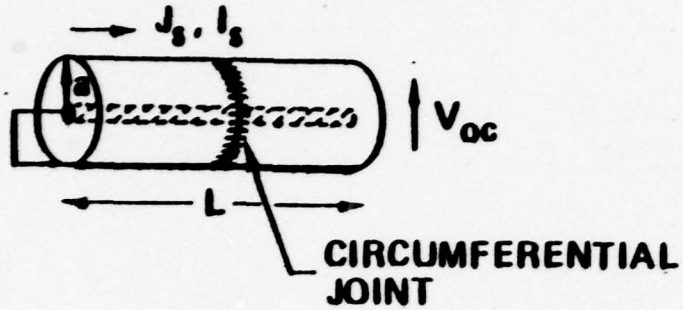

$$V_{oc} = V_J = \frac{J_s}{Y_J} = \frac{I_s}{2\pi a Y_J}$$

$$Y_J = \frac{I_s}{2\pi a V_J}$$

d) **Joints in leaky samples:**

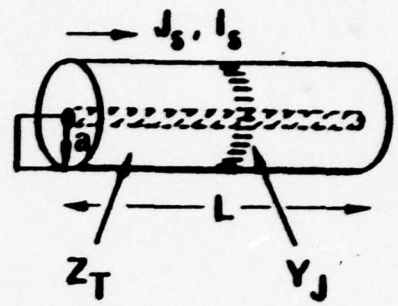

$$V_{oc} = I_s \left(Z_T L + \frac{1}{Y_J 2\pi a}\right)$$

$$Y_J^{-1} = 2\pi a \left(\frac{V_{oc}}{I_s} - Z_T L\right)$$

e) **Complete material specification:**

$$Z_T, Y_T, Y_J \longleftrightarrow z_{sd}, P, M, Y_J$$

Figure 6: Joint Admittance

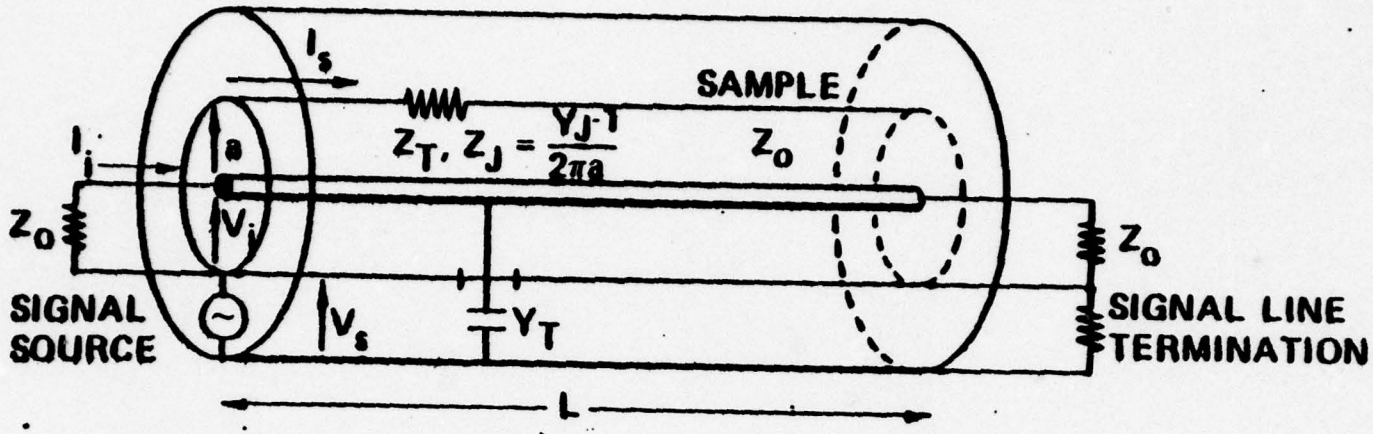

Z_T Coupling only:

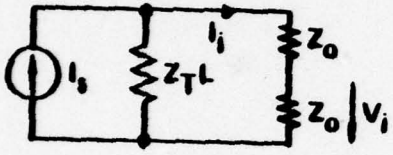

$$I_i = \frac{-V_i}{Z_o} = \frac{Z_T L I_s}{2 Z_o}$$

$$Z_T = \frac{2Z_o}{L} \frac{I_i}{I_s}$$

Y_J Coupling only:

LIKE Z_T COUPLING EXCEPT

$$Z_T L \rightarrow \frac{1}{Y_J 2\pi a}$$

$$Y_J^{-1} = 4\pi a Z_o \frac{I_i}{I_s}$$

Y_T Coupling only:

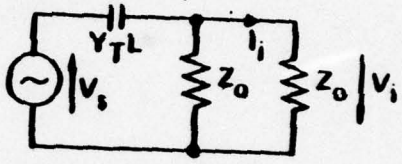

$$I_i = \frac{Y_T L V_s}{2}$$

$$Y_T = \frac{2}{L} \frac{I_i}{V_s}$$

Figure 7: Cylindrical Test Concept: Z_T, Y_T, Y_J

3.0 THEORETICAL FORMULATION

It is common [3-9] to formulate aperture coupling problems in terms of the tangential fields in the aperture. In particular, such problems can be formulated in terms of the tangential electric field $\hat{n} \times E$ in the aperture or the equivalent magnetic current density $\bar{J}_M = \bar{E} \times \hat{n}$ in the aperture [5,7,9]. It is also common to place the magnetic current over a conducting extension of the conducting sheet surrounding the aperture. In this case imaging requires a reduction in the effective magnetic current by a factor of two in order that the same aperture E-field be maintained[4,6,8]. This distinction has lead to substantial confusion and "factor of two" errors in previous studies involving aperture, material parameter, cable braid shielding, etc.

It has become common to describe small (electrically) aperture coupling in terms of equivalent dipole moments related to "outside" or "illuminated side" normal electric field E_n and tangential magnetic field H_t. This is illustrated in Figure 3. This idea has been generalized to allow description of shielding materials such as metal foils, screens or meshes, and composite laminates. Distributed apertures in meshes are described in terms of normalized electric and magnetic dipole moments per unit area or surface polarizabilities P & M. The penetrating tangential electric fields in solid materials are related to the "outside" current density J_s or magnetic field H_t by a constant surface transfer impedance z_{sd}. The distributed surface generalization condenses this to a surface transfer impedance z_s, containing both z_{sd} and M, and the surface electric polarizability P. This can be further condensed into a surface impedance operator $\bar{\bar{z}}_{sop}$ (Reference 9) containing both z_s and P.

$$\bar{\bar{z}}_{sop} \equiv \bar{\bar{z}}_s - \frac{\nabla_t P \nabla_t}{j2\omega\epsilon_o^2} \qquad (1)$$

where ∇_t is the transverse surface gradient differential operator, and $\bar{\bar{z}}_s$ is the tensor surface transfer impedance.

$$\bar{\bar{z}}_s \equiv \bar{\bar{z}}_{sd} + \frac{j\omega\mu_o\bar{\bar{M}}}{2} \tag{2}$$

For isotropic conductors and meshes $\bar{\bar{z}}_{sd}$ and $\bar{\bar{M}}$ are diagonal tensors described by the scalar parameters z_{sd} and M .

$$\bar{\bar{z}}_s \rightarrow (z_{sd} + \frac{j\omega\mu_o M}{2})\,\bar{\bar{I}} \tag{3}$$

where $\bar{\bar{I}}$ is the unit dyad. In rectangular coordinates:

$$\bar{\bar{I}} = \hat{x}\hat{x} + \hat{y}\hat{y} + \hat{z}\hat{z}$$

A detailed discussion of the basic material parameters and coupling mechanisms is contained in Reference (1). Part of this has been reproduced in this section for convenience.

The analysis generalizations described can be continued to include joints in surface materials as discontinuities in the surface transfer impedance in addition to the joint voltage differential description already described. As indicated in Reference 9, a discontinuity in the P description requires the introduction of an equivalent joint voltage in addition to the operator description $\bar{\bar{z}}_{sop}$.

$$\Delta V_p = \frac{\Delta P}{2\varepsilon_o} E_n \tag{4}$$

Here ΔP is the change in P across the discontinuity in the (assumed) direction of the external current density J_s, and E_n is the outward directed external normal E-field. The sense of the various voltages, currents, fields, etc. is illustrated in Figure 8. The generalization is completed with the joint impedance relation

$$\Delta V_j = Y_J^{-1} J_s \tag{5}$$

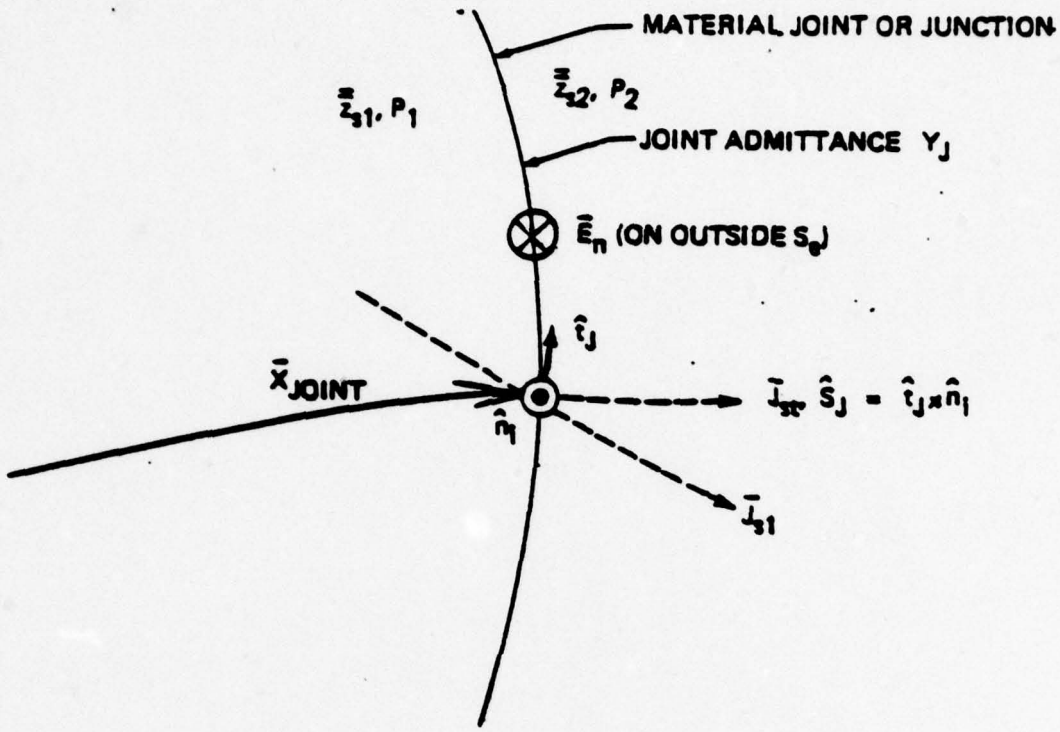

$$\bar{E}_J = \left(E_{tp} + E_{tJ}\right) \hat{S}_J$$

$$E_{tp} = \frac{\left(P_2 - P_1\right)}{2\varepsilon} E_n \; \delta\left(\bar{X}_{JOINT}\right)$$

$$E_{tJ} = \frac{\bar{J}_{sJ} \cdot \hat{S}_J}{Y_J} \; \delta\left(\bar{X}_{JOINT}\right)$$

$$\bar{E}_n = \hat{n}_1 \frac{\left(\nabla_t \cdot \bar{J}_{s1}\right)}{j\omega\varepsilon}$$

Figure 8: Material Joints

Gaps, non-conducting joints, and electrically long gaps between points of electrical connection must be treated as separate apertures since they do not lend themselves to the distributed joint coupling concept. Only good (or at least fairly good) conducting joints with a large number of points of good electrical contact per wavelength of joint width can be treated in the joint admittance concept.

The relation between the tangential electric field in a small aperture and the equivalent magnetic dipole moment is [5]:

$$\int_s E_t \, ds \equiv \int_s \bar{E} \times \hat{n} \cdot \hat{S}_J \, ds =$$

$$\frac{j\omega\mu M_s}{2} = \frac{j\omega\mu \, \alpha_{HS}}{2} J_s \tag{6}$$

Here E_t is the aperture tangential field directed along the prescribed moment axis $\hat{S}_J$, α_{HS} is the polarizability for the moment component $\bar{M} = M_s \hat{S}_J$. The corresponding geometry is shown in Figure 3.

Suppose next that a joint is considered to be formed of a narrow strip over which the surface tangential field is described. Alternatively, this might be viewed as a line aperture or a line of constituent small apertures; all such views are equivalent (Figures 3 & 4). Over any width W

$$\int_s E_t \, ds = \int_x^W \left[\int_y E_{ty} dy \right] dx = \int_x^W V(x) dx \tag{7}$$

the magnetic current surface integral is the line integral of the equivalent joint voltage V(x) which is in turn proportional

$$\int_x^W V(x) dx = \frac{j\omega\mu}{2} M(W) = \frac{j\omega\mu}{2} \sum_k^{N(W)} M_k \tag{8}$$

to the total dipole moment M(W) over W. Here N(W) is the number of constituent apertures with moment M_k contained in width W. The average joint voltage V_J is now obtained in terms of the dipole moment polarizability per unit length $\left\langle \frac{d\alpha}{dx} \right\rangle$.

$$V_J \equiv \frac{1}{W}\int_x^W V(x)dx = \frac{j\omega\mu}{2}\left(\frac{M(W)}{WJ_s}\right) J_s \tag{9}$$

$$V_J = \frac{j\omega\mu}{2}\left\langle\frac{d\alpha}{dx}\right\rangle J_s \tag{10}$$

Next, suppose the joint (perhaps a standard or calibration joint) were constructed of a line of regular apertures of known polarizability α_H and with relatively large and regular spacing of n aperturesper unit width. The distributed polarizability is now

$$\left\langle\frac{d\alpha}{dx}\right\rangle = n\alpha_H \tag{11}$$

so that $V_J = \frac{j\omega\mu n\alpha_H}{2} J_s$ (12)

and $Y_J^{-1} = \frac{j\omega\mu n\alpha_H}{2}$ (13)

Thus, it is possible to construct known inductive joint admittances for measurement calibration purposes. For example, consider a uniformly spaced array of small circular apertures of diameter D and spaced (S = 1/n) several diameters (S>>D). From Figure 3,

$$\alpha_H = \frac{D^3}{3}$$

and $Y_J^{-1} = \frac{j\omega\mu D^3}{6S} \equiv j\omega L_J$ (14)

Also, if the apertures are thin rectangular slots of width W and spacing S >> W, then

$$\alpha_H \equiv \frac{\pi W^3}{12\langle\ln\rangle}; \quad \langle\ln\rangle \equiv \ln\frac{2W}{\delta} - 1 \tag{15}$$

Here δ is the slot gap width at its center. If the apertures are elliptical then

$$\langle\ln\rangle = \ln\frac{4W}{\delta} - 1 \tag{16}$$

As a numerical example, suppose the circular apertures have (in, say, 5 mil copper) D = 2.5 mm

S = 7.5 mm ($n = S^{-1}$ = 133.3 holes/meter)

then the inductance of a 1 m. wide joint is

$$L_J = 4.36 \times 10^{-13} \text{ Hy. M.} \tag{17}$$

and

$$Y_J = j \frac{3.65 \times 10^5}{f_{MHz}} \ \mho/m \tag{18}$$

or

$$Y_J = j\ 365\ \mho/m \text{ at } 1000 \text{ MHz}$$

4.0 MEASUREMENT SCHEMES EVALUATED

4.1 The Quadraxial Test Concept

The quadraxial test concept, while somewhat difficult and costly to use because of its specific cylindrical nature and its requirement for expensive cylindrical samples, has a past history of joint and material parameter measurement. It has achieved the highest dynamic range and sensitivities known for these measurements. It's specialized geometry is amenable to precise analysis so that analytical reduction of measured data to parameter data is quite accurate. For these reasons the quadrax serves as a standard of comparison for the other measurement concepts considered.

The response of the quadrax as a function of material and joint parameters along with error functions and estimates has been thoroughly developed in reference 1. A portion of that development is reproduced here to establish an analysis base for the various measurement concepts treated.

The relationship of the material parameters z_s and P to the quadrax variables Z_T and Y_T is given in Figure 5. Schematically, the quadrax and its responses can be represented as shown in Figure 9.

In the standard configuration, the drive line (V_o, I_o, Z_{oD}, γ_D) is driven with I_{IN} at x = 0 and matched with a load Z_{oD} at x = L. The sense line (V_1, I_1, Z_o, γ) is matched with Z_o at both x = 0 and x = L. Coupling between the lines occurs via the distributed transfer impedance Z_{TQ} (ohms/meter of sample length) and transfer admittance Y_{TQ} (mhos/meter). The characteristic impedance and propagation factors of each line are respectively, Z_o, γ (sense line) and Z_{oD}, γ_D (drive line).

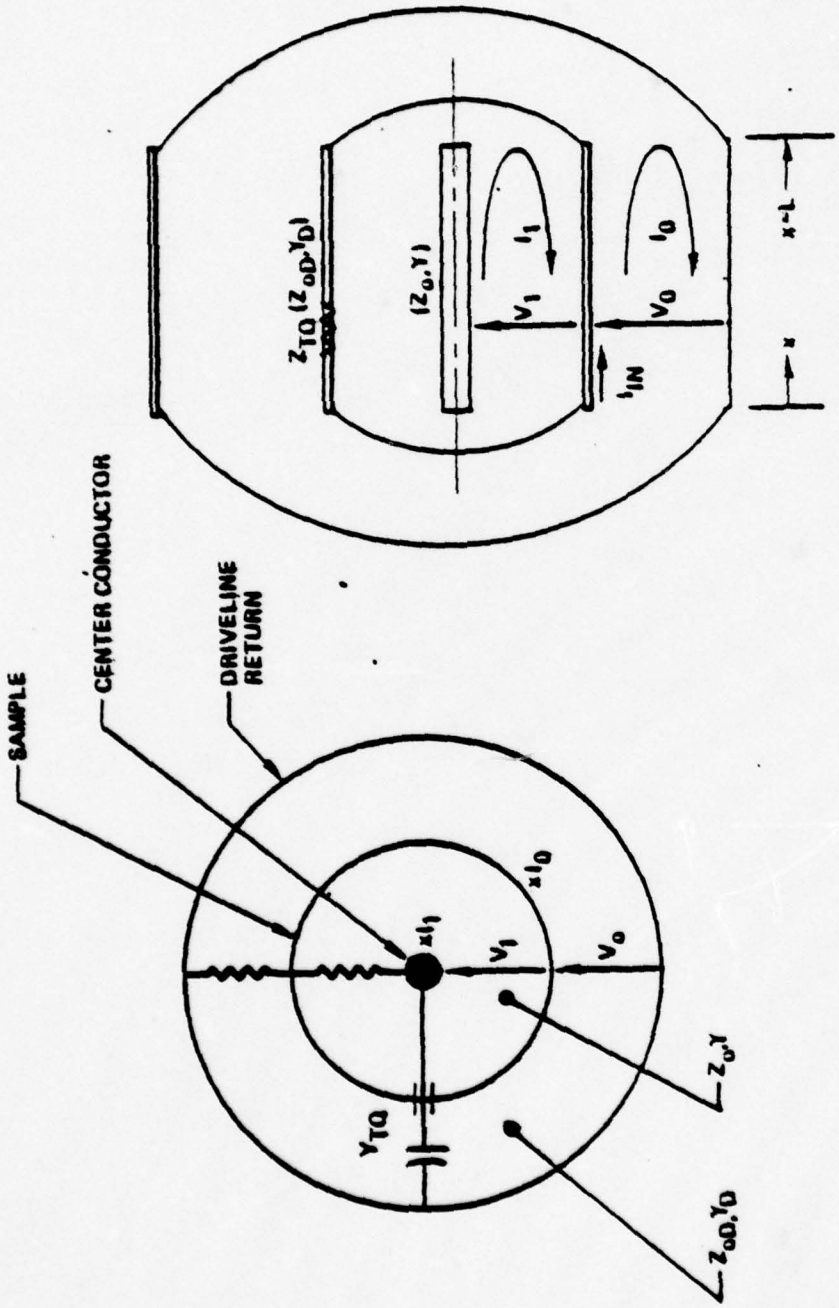

Figure 9: Quadrax Geometry

The Z_T and Y_T for the sample cylinder can be determined from the sense line responses at x = 0 and x = L. Those responses can be written in terms of the coupled line analysis in the sections II and III of reference 1. Excited line response is given as a function of position x and general drive and sense line terminations for Z_T coupling only and for Y_T coupling only. The total solution is obtained by superimposing these constituent solutions.

Specializing the solutions of reference 1 to the matched conditions assumed for the quadrax the total sense line responses become:

$$V_1(0) = \frac{1 - \varepsilon^{-(\gamma_1 + \gamma_0)L}}{2(\gamma_1 + \gamma_0)} \left[Y_T Z_{01} Z_{00} - Z_T\right] I_{IN} \tag{19}$$

$$V_1(L) = \frac{\varepsilon^{-\gamma_0 L} - \varepsilon^{-\gamma_1 L}}{2} \left[Y_T Z_{01} Z_{00} + Z_T\right] I_{IN} \tag{20}$$

Considering the relative positive polarities and definitions of Sections II and III[1] and quadrax diagrams:

$$\begin{aligned} Z_T &\longrightarrow Z_{TQ} & Z_{00} &\longrightarrow Z_{0D} \\ Y_T &\longrightarrow -Y_{TQ} & & \\ & & Z_{01} &\longrightarrow Z_0 \\ \gamma_1 &\longrightarrow \gamma & & \\ \gamma &\longrightarrow \gamma_D & & \end{aligned} \tag{21}$$

and

$$V_1(0) = \frac{L}{2} \varepsilon^{\frac{-(\gamma + \gamma_D)L}{2}} \frac{\sinh\left(\frac{\gamma + \gamma_D}{2} L\right)}{\left(\frac{\gamma + \gamma_D}{2} L\right)} \left[Y_{TQ} Z_0 Z_{0D} + Z_{TQ}\right] I_{IN} \tag{22}$$

$$V_1(L) = -\frac{L}{2} \varepsilon^{\frac{-(\gamma + \gamma_D)L}{2}} \frac{\sinh\left(\frac{\gamma - \gamma_D}{2} L\right)}{\left(\frac{\gamma - \gamma_D}{2} L\right)} \left[Y_{TQ} Z_0 Z_{0D} - Z_{TQ}\right] I_{IN} \tag{23}$$

For the present purpose the two quadrax transmission lines can be considered lossless with unit velocity factor so that

$$\gamma = \gamma_D = jk_o = j\frac{2\pi f}{c} \tag{24}$$

when jk_o is the propagation factor of light in space, f is frequency in Hertz and c is the velocity of light in space. The sense line responses become for this case:

$$V_1(0) = \frac{L}{2}\,\epsilon^{-jk_oL}\,\frac{\sin k_oL}{k_oL}\left[Y_{TQ}Z_oZ_{oD} + Z_{TQ}\right]I_{IN} \tag{25}$$

$$V_1(L) = \frac{-L}{2}\,\epsilon^{-jk_oL}\left[Y_{TQ}Z_oZ_{oD} - Z_{TQ}\right]I_{IN} \tag{26}$$

Note that for electrically short quadrax samples $k_oL << 1$ and (25) and (26) reduce to:

$$V_1(0) = -\frac{(Y_{TQ}Z_oZ_{oD} + Z_{TQ})L}{2}\,I_{IN} \tag{27}$$

$$V_1(L) = -\frac{(Y_{TQ}Z_oZ_{oD} - Z_{TQ})L}{2}\,I_{IN} \tag{28}$$

Notice that, in this case, the contribution of Y_{TQ} is symmetric with respect to the line ends while that due Z_{TQ} is antisymmetric. As the electrical length increases equation (25) shows the effect of destructive interference of the contributions to the $V_1(0)$ response due to excitation at the near ($x \doteq o$) and far ($x \doteq L$) ends of the sample. This effect is evident in the multiplicative factor $\frac{\sin k_oL}{k_oL}$.

Z_{TQ} and Y_{TQ} can be determined from (25) and (26) given $V_1(0)$, $V_1(L)$, I_{IN}.

$$Z_{TQ} = -\frac{\varepsilon^{jk_oL}}{LI_{IN}}\left[V_1(0)\frac{k_oL}{\sin k_oL} - V_1(L)\right] \tag{29}$$

$$Y_{TQ} = -\frac{\varepsilon^{jk_oL}}{Z_oZ_{oD}LI_{IN}}\left[V_1(0)\frac{k_oL}{\sin k_oL} + V_1(L)\right] \tag{30}$$

Or for small sample electrical length

$$Z_{TQ} \doteq -\frac{1}{L}\left[\frac{V_1(0)}{I_{IN}} - \frac{V_1(L)}{I_{IN}}\right] \tag{31}$$

$$Y_{TQ} \doteq \frac{1}{Z_oZ_{oD}L}\left[\frac{V_1(0)}{I_{IN}} + \frac{V_1(L)}{I_{IN}}\right] \tag{32}$$

Fine meshes tend to exhibit a considerably larger response due to Z_{TQ} than to Y_{TQ}. In this case, $V_1(0) \doteq -V_1(L)$ and measurement errors tend to be exaggerated when (30) is used to compute Y_{TQ}. An alternate measurement method can be used here. If an electrically short sample is employed with the drive line open circuited, the effect of Z_T is negated since I_o vanishes. The sense line responses are now:

$$V_1(0) \doteq V_1(L) \doteq \frac{-Y_{TQ}LZ_oV_o}{2} \tag{33}$$

or if the sense line is open circuited at $x = L$

$$V_1(0) \doteq -Y_{TQ}LZ_oV_o$$

so that Y_{TQ} is given by the voltage transfer ratio

$$Y_{TQ} = -\frac{1}{Z_oL}\frac{V_1(0)}{V_o} \tag{34}$$

Commonly, Y_{TQ} corresponds to a frequency independent capacitance so that a measurement at one frequency will suffice in that case. The short electrical length limitation can be removed by calculating Y_{TQ} from $V_1(0)$ and $V_1(L)$ using a form derived from the general coupled line solution in reference 1 with the drive line open circuited at x = L.

If the drive and sense lines are open circuited at x = L the general results reduce to:

$$\frac{V_1(0)}{V_{IN}} = \frac{Z_o L \varepsilon^{-\gamma L}}{2 \cosh \gamma L} \left[\left(1 + \frac{\sinh 2\gamma L}{2\gamma L}\right) Y_T + \frac{Z_T}{Z_{oD} Z_o} \left(1 - \frac{\sinh 2\gamma L}{2\gamma L}\right) \right] \quad (35)$$

When the common propagation factor $\gamma = jk_o$ (air dielectric), (35) becomes, in terms of Z_{TQ} and Y_{TQ}:

$$\frac{V_1(0)}{V_{IN}} = \frac{Z_o L \varepsilon^{-jk_o L}}{2 \cos k_o L} \left[-\left(1 + \frac{\sin 2k_o L}{2k_o L}\right) Y_{TQ} + \frac{Z_{TQ}}{Z_{oD} Z_o} \left(1 - \frac{\sin 2k_o L}{2k_o L}\right) \right] \quad (36)$$

For small electrical sample length ($k_o L < 1$), (36) becomes approximately:

$$\frac{V_1(0)}{V_{IN}} \doteq -Y_{TQ} L Z_o + \frac{Z_{TQ} L}{Z_{oD}} \frac{(k_o L)^2}{2} \quad (37)$$

Equation (37) indicates the suppression of the Z_T contribution to the sense line response for small $k_o L$. In this case, Y_T can be calculated from (37) using an estimate of Z_T to calculate the "error term" $\frac{Z_{TQ} L (k_o L)^2}{2 Z_{oD}}$

A more precise approach is possible which allows suppression of the Z_T contribution at small and intermediate electrical lengths. It involves matching both sense ports but open circuiting the drive line at x = L. Both

sense line responses are used in the calculation of Z_T and Y_T. Again specializing the general solution as indicated with $\gamma_D = \gamma_o = \gamma$ the sense line responses become:

$$V_1(0) = \frac{V_{IN}L}{4\cosh\gamma L}\left[\frac{Z_T}{Z_{oD}}\left(\varepsilon^{-\gamma L} - \frac{\sinh\gamma L}{\gamma L}\right) + Y_T Z_o\left(\varepsilon^{-\gamma L} + \frac{\sinh\gamma L}{\gamma L}\right)\right] \quad (38)$$

$$V_1(L) = \frac{V_{IN}L\varepsilon^{-\gamma L}}{4\cosh\gamma L}\left[\frac{Z_T}{Z_{oD}}\left(\varepsilon^{\gamma L} - \frac{\sinh\gamma L}{\gamma L}\right) + Y_T Z_o\left(\varepsilon^{\gamma L} + \frac{\sinh\gamma L}{\gamma L}\right)\right] \quad (39)$$

For small k_oL ($|\gamma L| << 1$) (38) and (39) reduce to

$$V_1(0) = \frac{V_{IN}L}{2Z_{oD}}\left(Y_T Z_o Z_{oD} - Z_T\frac{\gamma L}{2}\right) \quad (40)$$

$$V_1(L) = \frac{V_{IN}L}{2Z_{oD}}\left(Y_T Z_o Z_{oD} + Z_T\frac{\gamma L}{2}\right) \quad (41)$$

indicating the suppression of Z_T. The solution for Z_T and Y_T from (38) and (39) is, in matrix form,

$$\begin{bmatrix} Z_T/Z_{oD} \\ Y_T \quad Z_o \end{bmatrix} = \frac{-\gamma\cosh\gamma L}{V_{IN}\sinh^2\gamma L}\left[\begin{array}{c|c} \varepsilon^{\gamma L} + \frac{\sinh\gamma L}{\gamma L} & -\varepsilon^{\gamma L} - \frac{\sinh\gamma L}{\gamma L} \\ \hline -\varepsilon^{\gamma L} + \frac{\sinh\gamma L}{\gamma L} & \varepsilon^{-\gamma L} - \frac{\sinh\gamma L}{\gamma L} \end{array}\right]\begin{bmatrix} V_1(0) \\ \varepsilon^{\gamma L}V_1(L) \end{bmatrix} \quad (42)$$

Joint Admittance per Unit Width (Y_J):

Following the notation used in the last subsection, the response to a centered uniform point Y_J in a sample cylinder of radius a can easily be shown to be:

$$\begin{Bmatrix} V_1(0) \\ V_1(L) \end{Bmatrix} = \begin{Bmatrix} - \\ + \end{Bmatrix} \frac{\varepsilon^{-(\gamma+\gamma_D)\frac{L}{2}}}{4\pi a\, Y_J} I_{IN} \quad (43)$$

For the essentially lossless — unit velocity factor quadrax, the exponential contributes only phase delay.

$$\varepsilon^{-(\gamma + \gamma_D)\frac{L}{2}} \longrightarrow \varepsilon^{-jk_0L} = \varepsilon^{-j\frac{2\pi L}{\lambda}} \tag{44}$$

For low frequencies ($k_0L<<1$), is seen to reduce to the form of (27) and (28) with zero equivalent Y_T and with $Z_{TQ}L$ replaced by $(2\pi a\ Y_J)^{-1}$.

4.2 The Stripline Test Concept

One form of stripline test facility, applicable to both joint and material data, has been developed by SRI (10). It is depicted in Figures 10 and 11. This system is analytically very similar to the quadrax but uses flat plate samples instead of cylindrical ones. The sample leakage provides coupling between two matched transmission lines. The sample is limited in size to a faction of the line cross sectional perimeter so that the sample leakage signal and, hence, the system sensitivity are somewhat limited relative to the quadrax which uses the full perimeter of both lines. Further, the stripline has additional joints between sample edges and the facility (parallel to the primary current direction) which potentially limit sensitivity or dynamic range. Use of the SRI system has been limited to the approximate frequency range 10 kHz - 100 MHz. This system, like the quadrax, is limited in sensitivity at low frequencies by ground loop leakage in signal cabling connection to the stripline, signal source, and the leakage measurement systems. This problem can be eliminated by breaking ground loops with fiber optics or dielectric waveguide transducers. The high frequency end is limited by uniform field errors due to cavity and line resonances in the central stripline regions. These effects can be reduced by reducing stripline "working volume" size, increasing the transition taper lengths, and adding microwave type absorber in the transition regions. Working volume reduction will limit sample size but will not affect sensitivity as long as the cross sectional scale (Figure 10) does not change. The latter is set, essentially, by the design characteristic impedance (50Ω).

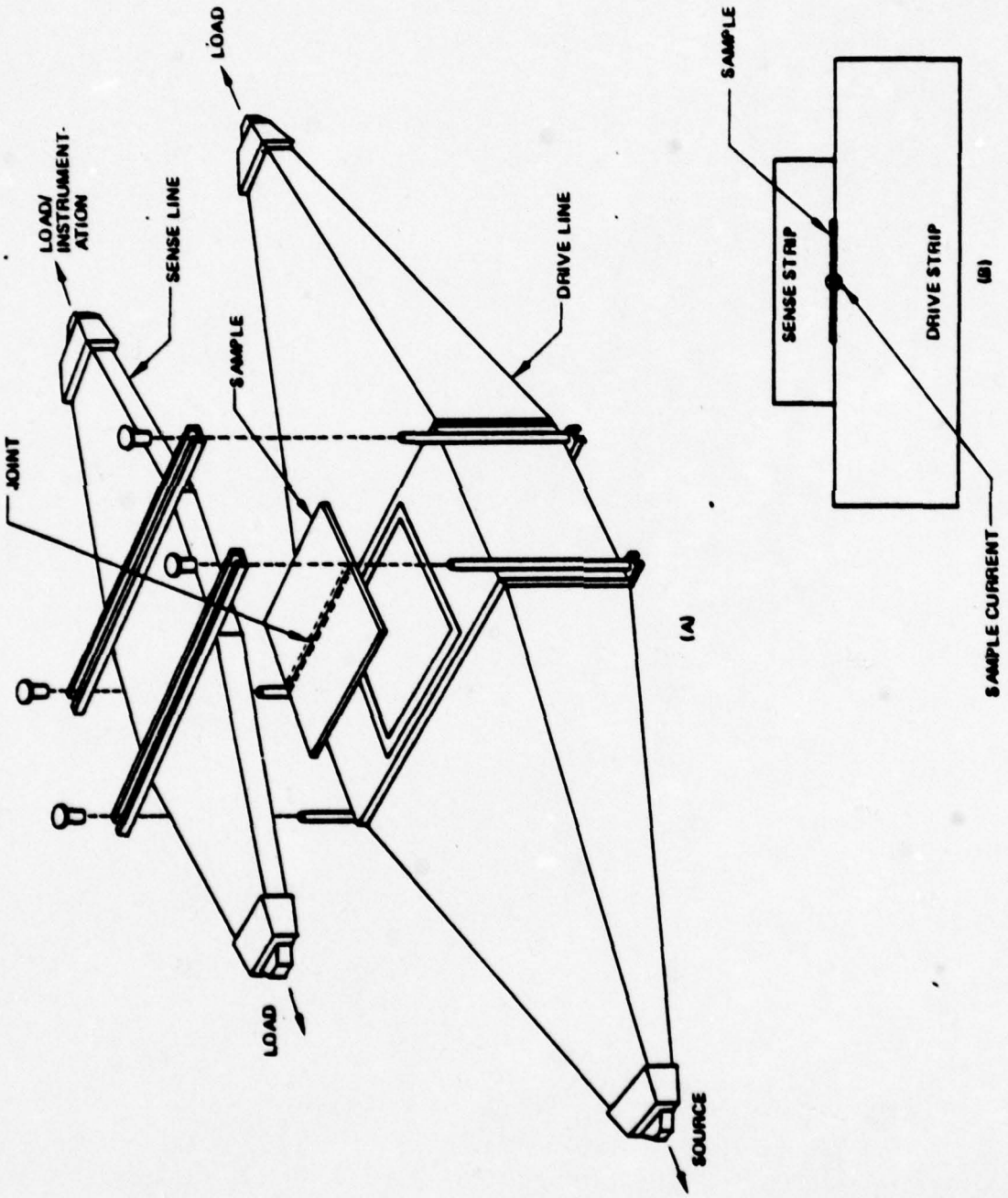

Figure 10: Stripline Facility

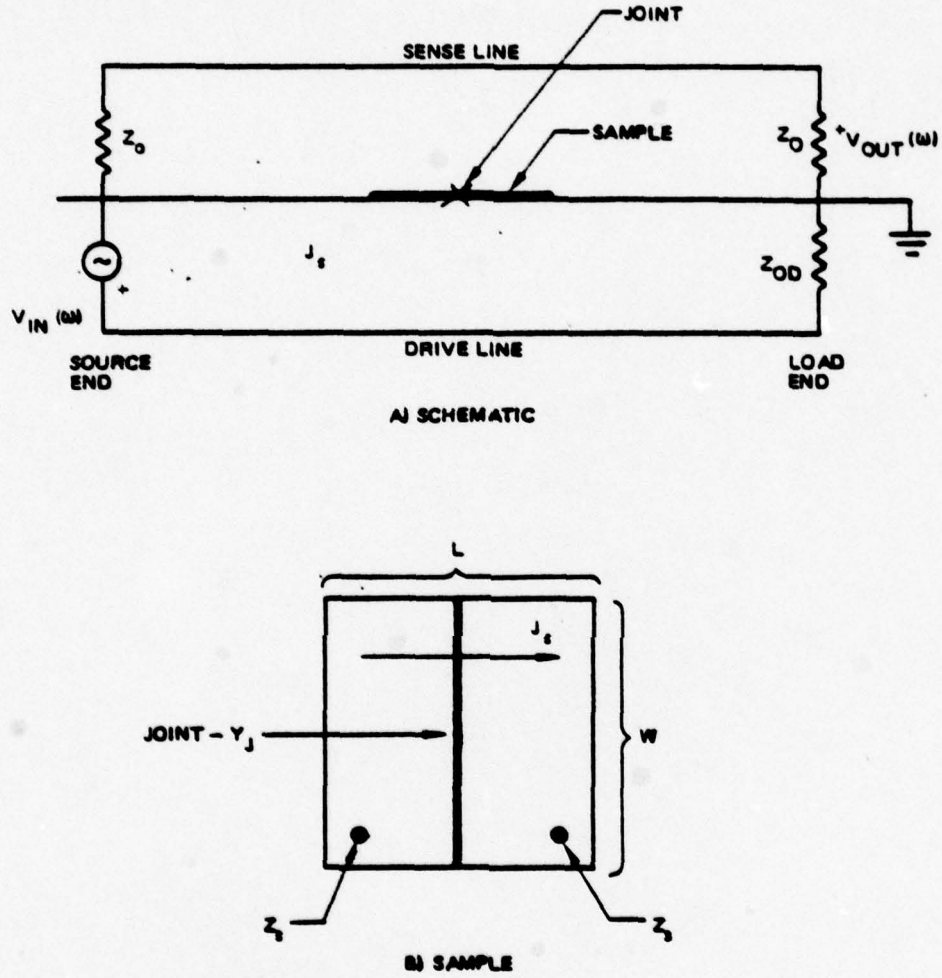

Figure 11: Stripline Concept

The quadrax response ratio, in terms of the stripline variables of Figure 11, is, from the preceding section:

$$R_a = \frac{V_{out}}{V_{in}} = \begin{cases} \dfrac{Y_J^{-1} J_s}{2 V_{in}} = \dfrac{Y_J^{-1}}{2 Z_{oD} \text{ cir}} & \text{(joints)} \quad (45) \\[2ex] \dfrac{z_s L J_s}{2 V_{in}} = \dfrac{z_s L}{2 Z_{oD} \text{ cir}} & \text{(short material samples)} \quad (46) \end{cases}$$

Here cir is the cylindrical sample circumference and L is the electrically short material sample length. For the stripline, these equations become

$$R_s = \frac{V_{out}}{V_{in}} = \frac{K}{2 Z_{oD} \text{ cir } 1} \qquad \begin{Bmatrix} Y_J^{-1} \\ Z_s L \end{Bmatrix} \begin{matrix} \text{(joints)} & (47) \\ \text{(material)} & (48) \end{matrix}$$

Again, L is the material sample length along J_s. K is a factor, less than unity, reflecting the fact that, since the sample does not surround the striplines, only part of the drive current flows on the sample and only part of the sample voltage is transferred to the sensing line. From inspection of Figure 10, K can be seen to be roughly

$$K \doteq \frac{W}{\text{cir } 2} \qquad (49)$$

with W the sample width and cir($\frac{1}{2}$) the circumferences of the driving and sensing strip. It is possible to make K fall in the range 1/3 to 1/10. This means that (disregarding the various system leakage or coherent noise effects) the stripline system is at best 10 to 20 dB less sensitive than the quadrax.

SRI states that (considering all coherent and incoherent leakage effects) with a transmitted power of 500 watts a voltage ratio (R) of 0.7×10^{-5} (-103 dB) was the minimum usable measurement. Since no reference to receiver sensitivity is made it is assumed that coherent noise or leakage around the sample dominated receiver noise. If cir($\frac{1}{2}$) and W for this case is taken as 1.2, 2.5, and .4 meters, respectively, with a K of 1/3, limits on measurable Y_J and z_s can be estimated as follows:

The reference voltage V_L in this case was taken from an H (J_s) loop A_L (4 in^2) in the drive line.

$$V_L = s\mu A_L J_s$$

and

$$R = \frac{W}{2\, s\mu A_L \text{ cir } 2\, Y_J} \equiv \frac{V_{out}}{V_L} \tag{50}$$

The maximum Y_{JM} and minimum z_{sm} measurable become

$$Y_{JM} = \frac{7.0 \times 10^5}{f_{MHz}} \quad (\mho/m)$$

$$z_{sm} = 2.9 \times 10^{-6} \quad (\Omega) \tag{51}$$

The most leaky joint imaginable would be a thin slot of full sample width. The dynamic range D.R. is given by the ratio of the responses of the most leaky and best measurable joints. Equivalently, it is set by the ratio of the slot impedances of the two joints; $Z_{SL}\, W^{-1}$ and $Y_{JM}^{-1}\, W^{-1}$.

$$\text{D.R.} = 20 \log_{10} |Z_{SL}\, Y_{JM}|$$

where

$$Z_{SL} = \frac{s\mu\, \pi\, W^2}{16 \langle \ell n \rangle} \tag{52}$$

and

$$V_{SL} = Z_{SL}\, J_s \text{ or } Y_{JM}^{-1}\, J_s$$

$$\text{D.R.} = 20 \log_{10} \left| \frac{\pi\, W^3}{32 \langle \ell n \rangle R \text{ cir2 } A_L} \right| = 95 \text{ dB} \tag{53}$$

4.3 The "Flat-Plate Test" Concept

Another alternative means of material parameter measurement involving the use of thin planar material samples is "the flat-plate test." Provided that the material is essentially linear, homogeneous (at least piecewise homogeneous layers), and isotropic, all material properties can be obtained from flat-plate ESE and MSE measurements. These are measurements of the insertion loss provided by the planar material

sample when interposed midway between coaxial electric and magnetic dipoles, respectively. P is determined from the ESE measurement while z_s is determined from the MSE measurement. Usually, good shielding materials exhibit large ESE so that MSE is a good indicator of shielding material quality. The flat-plate MSE test geometry is described in Figure 12. MSE for homogeneous solid shells is given in terms of conductivity and shell dimensions. The MSE formula can be written alternatively in the conventional nomenclature of absorption loss, reflection loss, and re-reflection loss as indicated in Figure 12. In principle, one can calculate conductivity given the shield-test geometry and an MSE-frequency plot so that the material parameter z_s can be calculated. These formulas only hold for solid homogeneous shells. It is shown in reference 1 that z_s can be calculated from flat-plate MSE for a large class of inhomogeneous or pseudo-homogeneous materials such as fine wire meshes, graphite laminates, and graphite laminates coated with layers of mesh, metal foils, etc.

If the coils are small in terms of their distance to the plate yet close in terms of plate dimensions, the dipole approximation can be used to determine the fields produced and the response voltage V. With the plate removed the response voltage can be easily shown to be:

$$V_r = \frac{s \mu A^2 I}{16 \pi r^3} \; ; \; s \equiv j\omega \tag{54}$$

Where A is the loop area and I is the drive current (IA is the magnetic dipole moment of the driven coil). The ratio of the reference response voltage V_r to the coil voltage with the plate in place is the magnetic shielding ratio R_H - the magnitude of R_H expressed in dB is MSE. R_H can be shown to be

$$R_{Hz} = 1 + \frac{s \mu r}{3 z_s} \tag{55}$$

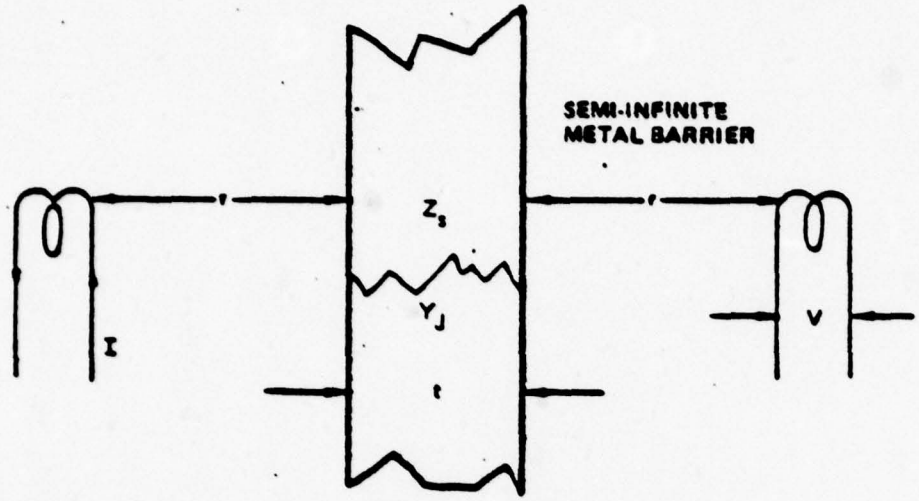

MSE = MAGNETIC SHIELDING EFFECTIVENESS = $20 \text{ LOG}_{10} \frac{V_1}{V_2}$ DECIBELS.

WHERE V_1 IS MEASURED WITH BARRIER ABSENT AND V_2 WITH BARRIER PRESENT, I BEING KEPT CONSTANT.

$$MSE = A + R_1 + R_2 \tag{1}$$

WHERE

$$A = \text{ABSORPTION LOSS (dB)} = 3.3 \times 10^{-3} t \sqrt{f\sigma\mu} \tag{2}$$

R_1 = REFLECTION LOSS (dB) =

$$20 \text{ LOG}_{10} \left[\frac{0.46}{r} \sqrt{\frac{\mu}{f\sigma}} + 0.14r \sqrt{\frac{\sigma f}{\mu}} + 0.35 \right] \tag{3}$$

R_2 = RE-REFLECTION LOSS (dB) =

$$10 \text{ LOG}_{10} \left[1 - (2 \times 10^{-0.1A}) (\cos 0.23A) + 10^{-0.2A} \right] \tag{4}$$

AND WHERE

- t = METAL THICKNESS (MILS)
- σ = CONDUCTIVITY RELATIVE TO COPPER
- μ = PERMEABILITY RELATIVE TO VACUUM
- r = SOURCE TO BARRIER DISTANCE (IN.)
- f = FREQUENCY (Hz)

Figure 12: Magnetic Shielding Effectiveness Equations For Flat Plate Test

The same configuration can be used on jointed plates. Assuming a straight line joint centered on the plate with joint admittance Y_J per unit length, the resulting shielding ratio would result (joint leakage dominant):

$$R_{HY} = 1 + \frac{32\, s\, \mu\, r^2\, Y_j}{45} \tag{56}$$

For either Y_J or z_s leakage, the output coil response and the shielding ratio(s) can be obtained using (54), (55), and (56). If both types of sample leakage exist, the total response is obtained by adding the constituent responses. The net shielding ratio R_H becomes:

$$(R_H - 1)^{-1} = (R_{Hz} - 1)^{-1} + (R_{Hy} - 1)^{-1} \tag{57}$$

or

$$R_H = 1 + \frac{s\, \mu\, r}{3\left[z_s + \frac{15}{32\, Y_J\, r}\right]} \tag{58}$$

If the coils are closely spaced from the plate ($r \ll d$) in terms of coil dimensions, another set of simple approximations apply. The coil plate proximity forces a somewhat different current distribution on the same and a different effective range factor r_e ($r \rightarrow r_e$) on the response expressions. The wire radius a used in the coil now effects the response unless $a \ll r \ll d$.

The reference response for the close loop becomes

$$V_r = sMI \pm \frac{s\, \mu\, d}{2} \ln \frac{2\, d}{r}\, I \tag{59}$$

where the mutual inductance of the coils M and r is determined from the coil centers to the plate position.

The plate current density is localized to the coil becoming maximum directly "under" the coil wire. It can be described locally like the 2 dimensional (2D) wire over ground shown in Figure 13. The 2D current density distribution over a good (perfect) conductor is

$$J_s(X) = \frac{I}{\pi h_e \left[1 + \frac{x^2}{h_e^2}\right]} \tag{60}$$

The effective resistance per unit length introduced into the wire circuit by a good but finite conductivity plane, assuming the current distribution (60) and a semi-infinite plane of uniform conductivity and surface impedance or resistivity R_s, can be shown to be

$$R = \frac{R_s}{2\pi h_e} \quad ; \; h_e^2 = h^2 - a^2 \tag{61}$$

For thin wire coils the effective height a range h_e of (60) and (61) reduce to the actual height h. Similarly, the transfer impedance per unit length from wire to wire (Figure 13c) is determined from the surface transfer impedance z_s as

$$Z_T = \frac{z_s}{2\pi h_e} \tag{62}$$

This form applies also to the loop to loop coupling of Figure 13d.

$$V_o = \pi d Z_T I = \frac{z_s d}{2 h_e} I \tag{63}$$

Including the effect of a centered linear joint Y_J

$$V_o = \frac{d}{2 h_e} \left[z_s + \frac{2}{\pi d Y_J}\right] I \tag{64}$$

The MSE shielding ratio R_H becomes

$$R_H = 1 + \frac{s \mu r_e}{3 \left[z_s + \frac{2}{CIR\, Y_J}\right]} \tag{65}$$

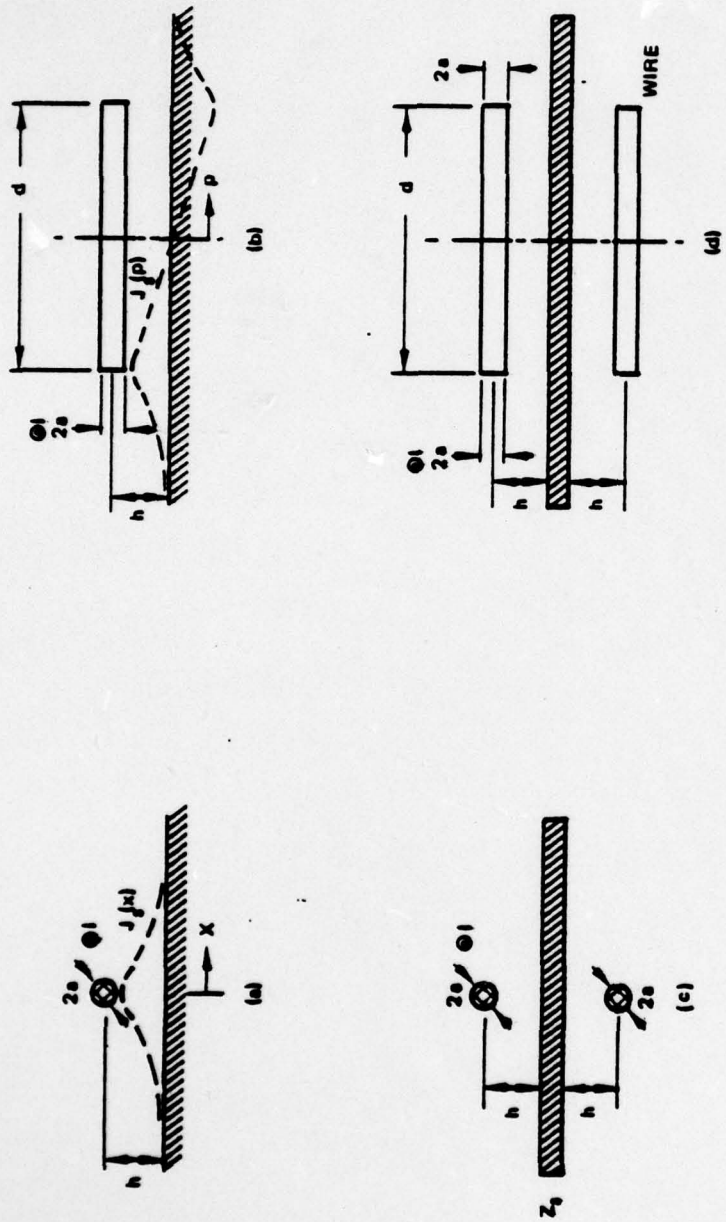

Figure 13: Close Conductor Proximity Effect

where $r_e = 3h_e \ln \frac{2d}{h_e}$

$cir = \pi d$

$h_e^2 = r^2 - a^2$

It is seen from (65) that, as one would expect from geometrical considerations, z_s and Y_J leakage terms are equivalent within the appropriate geometrical and dimensional scaling factors.

$$CIR\ z_s J_s \rightarrow (CIR\ z_s + \frac{n}{Y_J})\ J_s \tag{66}$$

This is expected since the transfer voltage due z_s is proportional to z_s and the current path length CIR while over the current path two (n=2) joint contributions of $Y_J^{-1} J_s$ are encountered. This equivalence between z_s and Y_J^{-1} exists in all joint or material measurement schemes; only the scale relation changes depending on active current path length and the number of times n the joint is encountered along that path. It was seen that for the remote loop the effective CIR was 1.36 times that where the maximum current density occurred (at $\rho_m = r/2$). This is reasonable since J_s rolls off more slowly for $\rho > \rho_m$ than for $\rho < \rho_m$. In the quadrax and stripline systems; the CIR factor is the sample length and n = 1 since the current encounters the circumferential joint only once.

4.4 The Anechoic Chamber

In this concept a simulated plane wave is directed normally onto the material sample. The leakage through the finite sample is a measure of the material parameters z_s and P as well as the joint admittance Y_J if the sample is jointed. In practice, the sample would be essentially square approximately 12-18 inches on a side and would be placed in the dividing partition of a small anechoic chamber as shown in Figure 14. The actual size of the chamber, the type and amount of wall mounted absorbing material, and the antennas used for

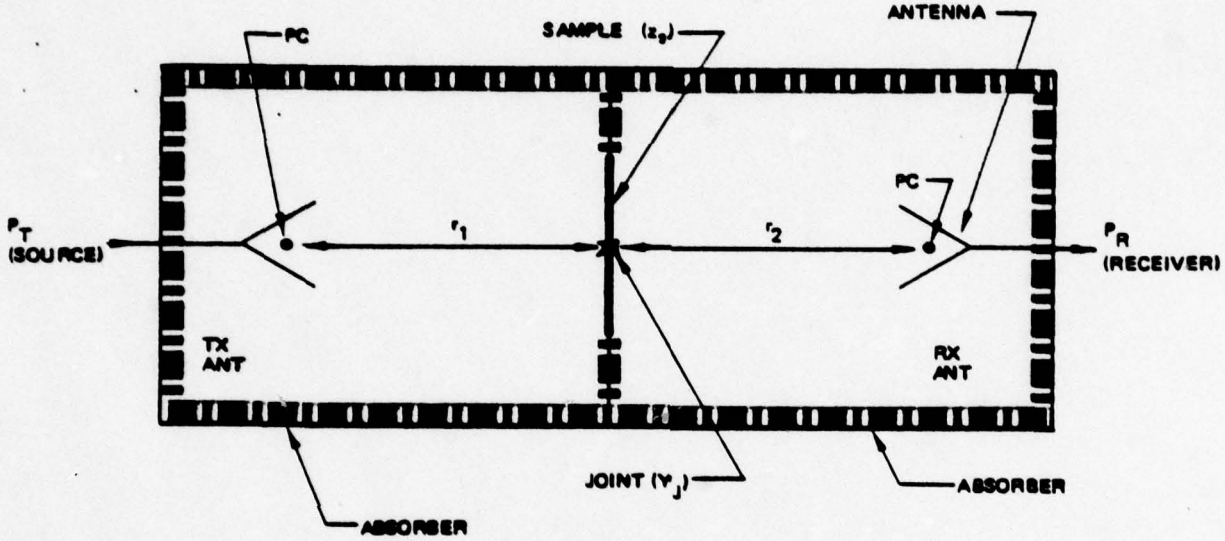

Figure 14: The Anechoic Chamber

sample illumination and leakage detection will depend on the intended frequency range and the desired dynamic range. The sample would be attached to the nontransmitting partition by joints of leakage small by comparison to that through the sample (and its central joint Y_J). The antennas would be either conventional horns or log periodic dipole arrays (LPDA) to increase the frequency range of a given antenna. A number of antennas would be required to cover the frequency range of a given facility.

For purposes of analysis of system response and dynamic range it will be assumed at first that the chamber interior walls are perfectly absorbing and that whatever antennas are used, an essentially uniform planar incident wave would be produced at the sample by energizing either antenna. The incident fields will be calculated using spherical radiation formulas, the standard gain and phase center (P.C.) of the antennas as indicated in Figure 14.

Joint Leakage (Y_J):

The incident power density S_i at the sample can be written in terms of the applied power P_T, the phase center range r_1, the transmitting horn gain G_{H1}, the peak incident electric field E_1, and the peak current density (J_s) induced on a good conducting sample.

$$S_i = \frac{P_T G_{H1}}{4\pi r_1^2} = \frac{E_1^2}{2\eta} = \frac{\eta J_s^2}{8} \tag{67}$$

or

$$J_s^2 = \frac{2 P_T G_{H1}}{\eta \pi r_1^2} \tag{68}$$

The intrinsic impedance of vacuum is denoted by η which is 120π. The sample joint will be considered equivalent to a slot radiator which is uniformly excited and produces a uniform slot voltage over the joint width. Such a "slot" would not exhibit resonances characteristic of the sample joint width because of essentially continuous shunt conductive loading (joint contact) and possible periodic shorts due to rivets, bolts, or other fasteners.

Of course, certain joints with essential gaps in loading between periodic tie points may exhibit resonance effects characteristic of the spacing between ties.

Following the indicated simplifying assumptions, the second horn response is written in terms of a sample produced energy density or Poynting's vector and its own effective aperture A_{H2} or equivalently its gain G_{H2}

$$P_r = \frac{A_{H2}}{2\,\eta\,\lambda^2\,r_2^2}\left[V_J\,W\right]^2 \tag{69}$$

where V_J is the slot voltage and W is its width (linear run as opposed to a gap). The slot voltage is related to the joint admittance and excitation current density in the standard manner. The ratio of received to transmitted power then becomes

$$\frac{P_r}{P_T} = G_{H1}\,G_{H2}\left[\frac{W}{2\pi\,\eta\;\;r_1 r_2\,Y_J}\right]^2 \tag{70}$$

If the receiving antenna were a large horn pushed up against the partition and centered on the sample, then the sample power radiated by side 2 is nearly totally absorbed by the horn. This approach was employed [9] to measure graphite transmissibility. It appears to improve the ratio of received transmitted power to leakage from other sources, in addition to increasing the sensitivity to maximum. The sensitivity (disregarding the obscuring effect of leakage) can be approximated by letting r_2 be the distance from the mouth or aperture of the horn to its phase center (P.C.).

Material Leakage (z_s)

Here the sample is assumed to be an infinite sheet. If the sample were removed, the received power would be:

$$\frac{P_R}{P_T} = \frac{G_{H1}\,A_{H2}}{4\pi\,(r_1 + r_2)^2} = G_{H1}\,G_{H2}\left[\frac{\lambda}{4\pi\,(r_1+r_2)}\right]^2 \tag{71}$$

If the sample is replaced, the midplane tangential electric E_t field is related to that with the sample removed as:

$$\frac{E_t^z}{E_t^{inc}} = \frac{2\, z_s\, H_t^{inc}}{\eta_o\, H_t^{inc}} = \frac{2\, z_s}{\eta_o} \tag{72}$$

The sensitivity ratio is then

$$\frac{P_R}{P_T} = G_{H1}\, G_{H2} \left[\frac{\lambda}{2\pi\,(r_1+r_2)} \frac{z_s}{\eta_o} \right]^2 \tag{73}$$

The above idealizations are not extremely accurate, because of incident field nonuniformity, but should suffice in comparative studies with other measurement systems. Nonuniformity errors result from wall reflections and proximity of antenna to the sample. Also, the sample is finite in size and edge (field truncation) effects modify the results. At this stage, it is unclear, due to limited specific experience with small chambers of this type, what the ultimate computational accuracy will be. At the outset, it appears preferrable to use canonical (standard) sheets and joints, whose effective z_s and Y_J are known by construction, as a standard of comparison. Unknown material z_s and joint Y_J are determined from the measured transfer functions by relating their responses to the response of the known standards. The easiest way of producing these standards is by cutting an array of canonical apertures in a thin conducting (copper) sheet. The coupling through (polarizability) electrically small apertures of circular, elliptical, or rectangular form is precisely understood and has been described in Sections 2.0 and 3.0. The surface and linear polarizabilities of rectangular and linear slot arrays (alternatively z_s and Y_J, respectively) are determined by multiplying the individual aperture polarity α by the appropriate surface or linear aperture number densities n_a and a packing factor f_p.

$$\left.\begin{aligned} \frac{d\alpha}{dA} &= \alpha \frac{dn}{dA}\, f_{pA} \qquad (74) \\ \frac{d\alpha}{dx} &= \alpha \frac{dn}{dx}\, f_{p\ell} \qquad (75) \end{aligned}\right\} \rightarrow \alpha\, n_a\, f_p$$

where

$$z_s = \frac{j\,\omega\,\mu}{2}\,\frac{d\alpha}{dA} \tag{76}$$

$$Y_J^{-1} = \frac{j\,\omega\,\mu}{2}\,\frac{d\alpha}{dx} \tag{77}$$

The factor f_p ranges from 0 to 1; it can be made very nearly unity by adequate slot spacing. Edge-to-edge spacings of 2 or more slot widths (maximum active dimension) are assumed to produce unit f_p. It has been assumed that the slots are cut in a sheet which is thin by comparison to the slot dimensions (widths). The effect of slot "thickness" or "depth" is to reduce α. Sheet thickness less than 1/10 the active slot dimension produces an insignificant effect. Analytical corrections are available[1].

5.0 CHARACTERISTICS OF EXISTING TEST FACILITIES

Most joint and material parameter measurement facilities are similar in concept to either the QUADRAX or Flat Plate MSE (FPT) measurement facilities used in the 0-100 MHz range on previous programs (1, 9). Since detailed performance data on each of the systems is available, it can be used as a standard of comparison for other proposed systems. The following section describes the QUADRAX and FPT measurement systems and their performance.

5.1 Magnetic Shielding Effectiveness Test (Flat Plate Facility)

The equations that define magnetic field shielding effectiveness (MSE) in terms of the test setup parameters are shown in Figure 12. The MSE of planar test specimens is defined as the ratio of two voltages (V_1/V_2) where V_1 is the voltage measured on the receive coil with the test panel absent and V_2 is the receive coil voltage with the test panel present. Figures 15 and 16 show the apparatus used to measure MSE. The test samples were 12-inch-by-12-inch flat plates. A photograph of the test setup is shown in Figure 17.

The test procedure that was used for obtaining the MSE of a material consists of comparing the output voltages of the receive coil obtained with and without the intervention of the sample under test. In the setup shown in Figure 15 the two measurements of the receive coil output voltages were accomplished simultaneously. One side of the shield box contained the test sample, while the other side had air between the drive and receive coils. Both sides of the shield box were built to be electrically and physically identical. The system was calibrated by removing the test sample and comparing the voltage output of the receive coils. The resulting curve was 0 dB shielding effectiveness.

The main part of the instrumentation system was the Hewlett Packard (HP) network analyzer, which consists of a sweep generator (HP8601), the network analyzer (HP8407) and the oscilloscope display unit (HP8412). This instrumentation system automatically sweeps the test frequency range and determines the ratio of the receive coil voltages, which is the MSE defined in Figure 12. The

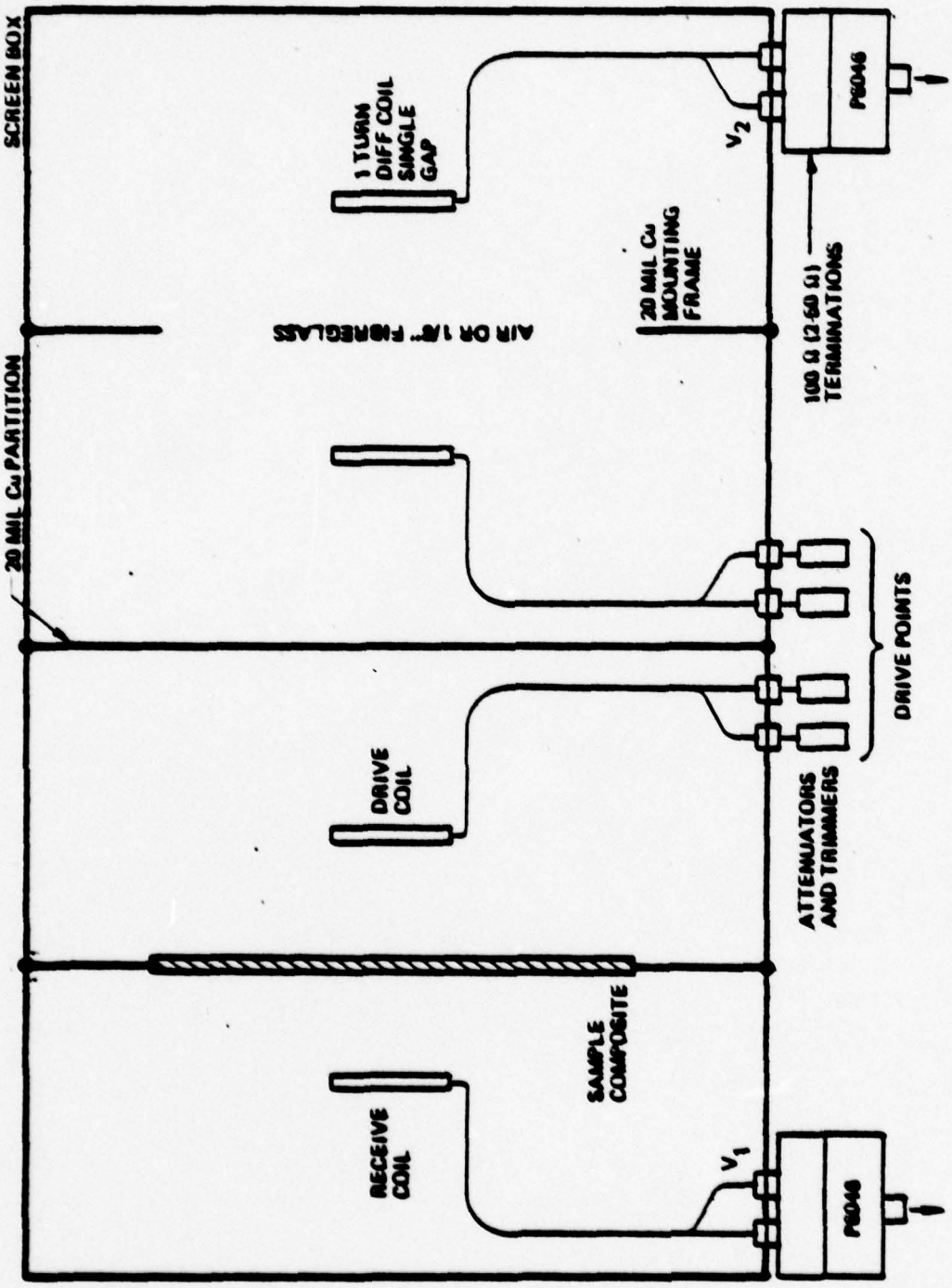

Figure 15: H-Field S.E. Test Setup

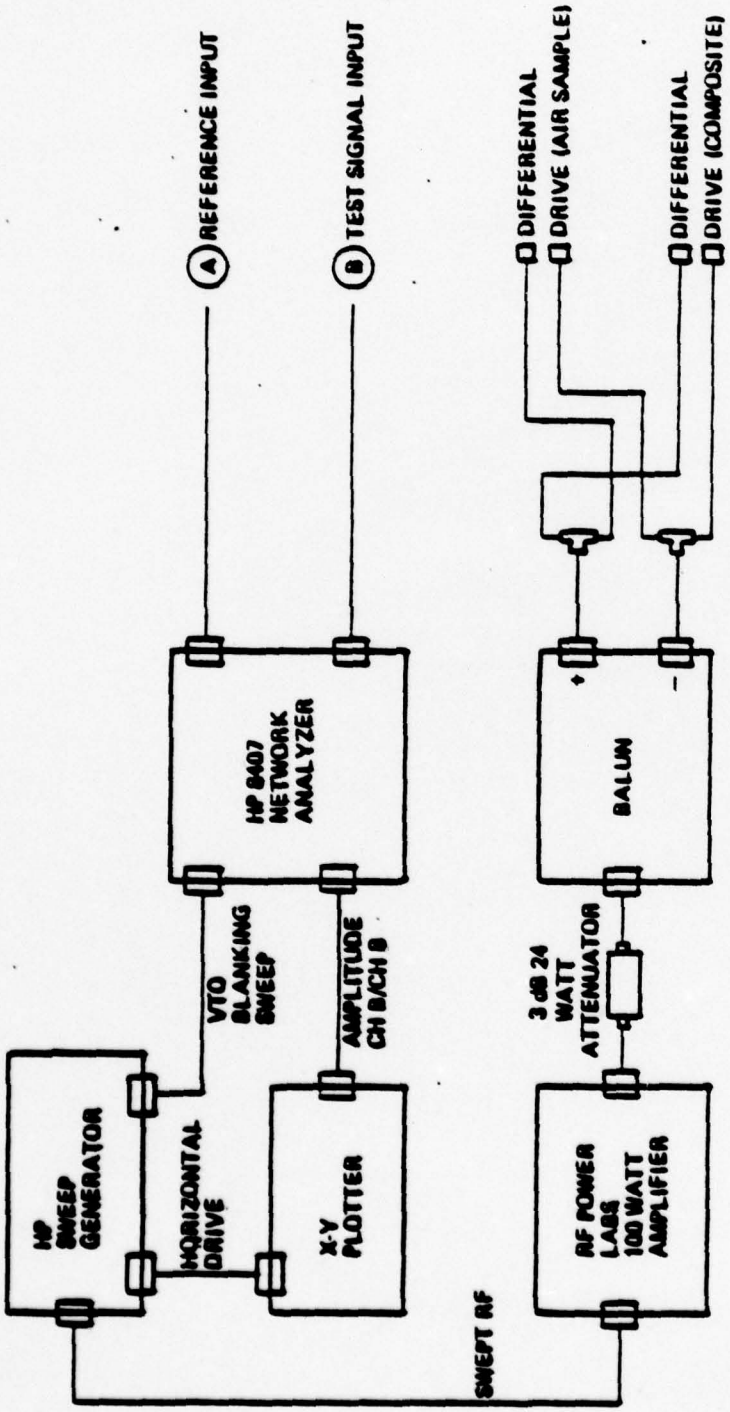

Figure 16: H-Field S.E. Test Instrumentation

Figure 17: Flat Plate S.E. Test Equipment

test data were obtained in three separate sweeps covering the 0.1 to 1, 0.1 to 10, and 9 to 10 MHz frequency bands.

For frequencies below 0.1 MHz, MSE data were obtained using an HP spectrum-analyzer/tracking-generator system and the instrumentation described above.

5.1.1 CW Driver

The CW source consisted of the HP8601 sweep generator and an RF power Labs 200-watt amplifier. Both units are designed to drive 50-ohm single-ended loads. The output of the power amplifier is connected to a balun through a 3-dB, 24-watt attenuator. The attenuator is required to limit the standing wave ratio to 3:1, to be compatible with the power amplifier. The balun is a step-down transformer providing current gain. It converts a single-ended input signal to a differential output. Coaxial "T"'s were used to power divide the differential signals to drive both sides of the shield box. Attenuators and short sections of coaxial lines were used at the shield box interface to compensate for slight imbalances in the drive system in the 10-to-100 MHz frequency range.

5.1.2 Shield Box

The shield box, made from 18-mesh phosphor bronze screen, contained two sets of coils. The coils were split-shield loop antennas made from 0.141-inch-diameter, copper-clad coaxial cable. The coils were one turn, one inch in diameter, and were placed 2 inches apart. Each set of coils was electrically isolated from the other other by a 20-mil-thick copper plate partition.

The coils nearest to the center partition were driven by the differential voltage source. The other two coils served as the receive antennas; one provided the reference signal to the network analyzer, the other the test channel input.

A copper frame was mounted at the center of both sides of the shield box. A hole, 11 inches square, was cut out of each frame. The RFI gasket was soldered around the periphery of the hole. The test sample was mounted against the RFI gasket. The electrical contact obtained by taping the test sample against the RFI gasket was sufficient to eliminate E-field coupling around the edges of the sample. Figure 18 is a photograph of the inside of the shield box with a test sample installed.

5.1.3 Monitoring Recording System

Tektronix P6046 differential probes were used to convert the voltage output of the receive coils to single-ended, 50-ohm sources to drive the network analyzer. The P6046 probes also provide a significant amount of common-mode rejection. Both inputs of each P6046 probe were terminated in 50 ohms.

The P6046 probe which measures the receive coil on the test-sample side was additionally shielded (probe, probe cable, power supply and amplifier) to eliminate stray RF pickup which at first limited MSE measurements to a 60-dB dynamic range. The HP network analyzer automatically determines the ratio of the two output signals from the P6046 probes and displays the results on its oscilloscope display unit. The network analyzer also provides the output for an x-y plotter which was used to record the test data. A separate frequency counter was used to calibrate the horizontal sweep (frequency) of the x-y plots because the horizontal drive signal of the sweep generator was not linear in the 0.1 to 0.5 MHz range and in the first decade of frequency for sweep ranges of 0.1 to 10 MHz and 1 to 100 MHz.

5.1.4 Test Setup Evaluation

Numerous tests were conducted to evaluate the performance of the MSE test system. The significant data from these tests are shown in Figure 19 for the 1 to 100 MHz frequency band (the worst-case frequency range). The curve labeled "A" corresponds to the 0-dB calibration of the network analyzer. Curve B

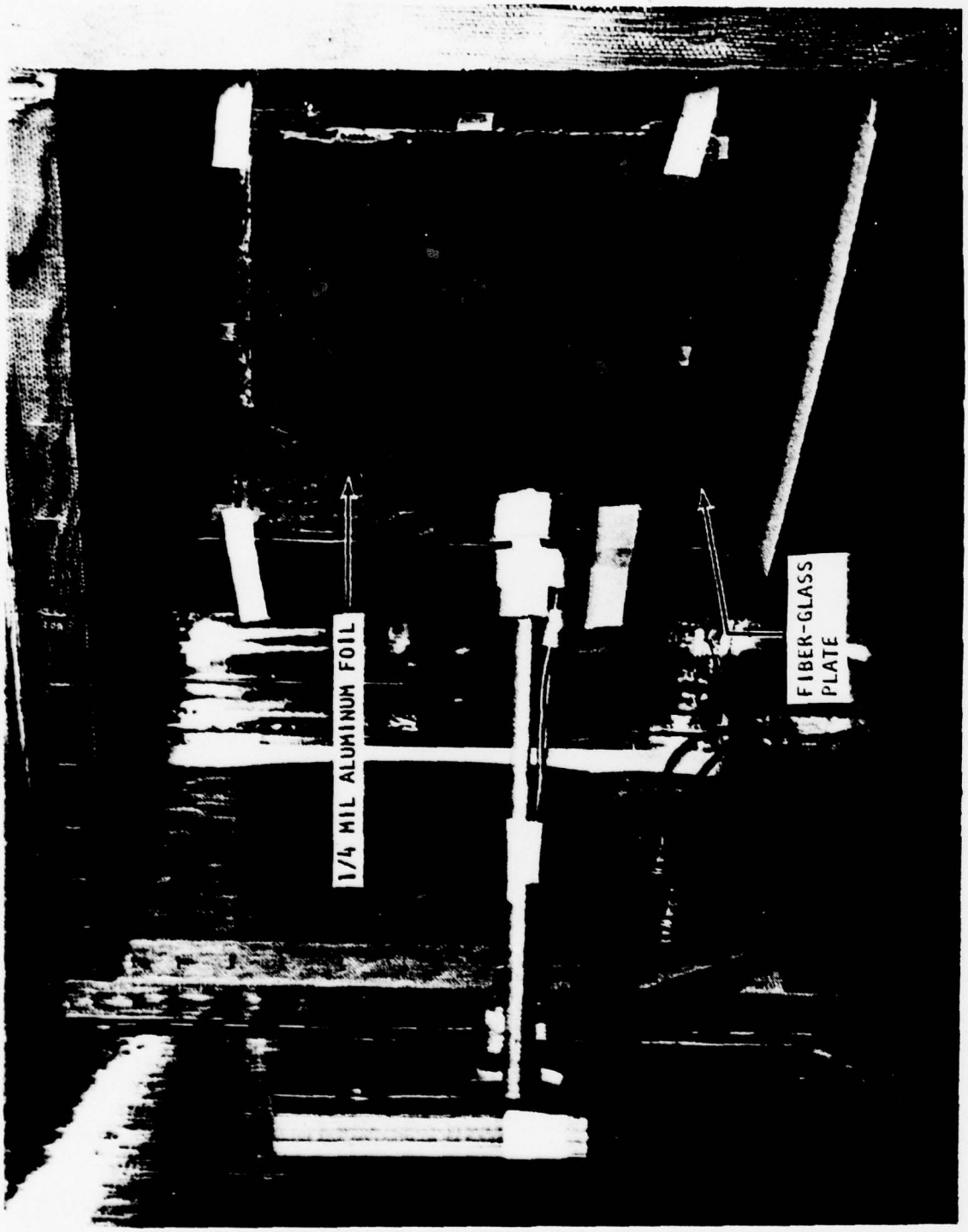

Figure 18: Test Sample in Screen Box

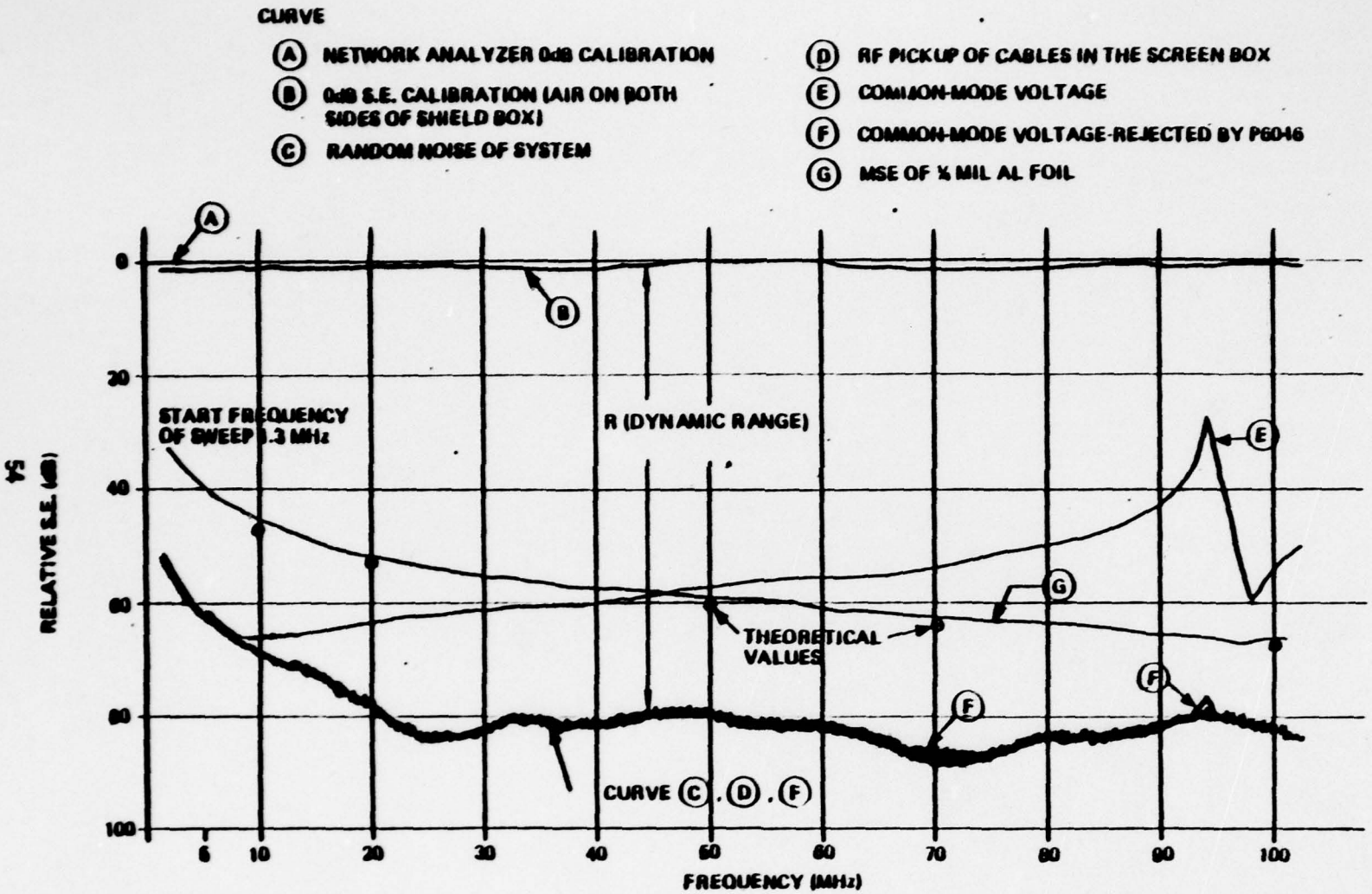

Figure 19: MSE Test System Evaluation Data

is the 0-dB MSE calibration of the test setup (air sample on both sides of screen box) which varies about 2 dB across the test frequency range.

Curve C corresponds to the random noise of the test system. The receive coil output cables were disconnected from the P6046 at the shield box interface on the test-sample side for this measurement. Curve D represents the RF pickup of the cables which connect the P6046 probe to the receive coil (receive coil disconnected on the sample side) inside the shield box. Curves C and D are nearly the same and represent the ultimate sensitivity of the system. For test frequency ranges 0.1 to 10 MHz and 10 to 100 kHz, two other baluns are used to improve the sensitivity of the test system.

Because of small imbalances in the drive system and electric field coupling between the drive and receive coil, there was a detectable common-mode voltage present at the receive coil outputs. Curve E was the common-mode voltage measured at the shield box interface using a P6046 in a single-ended configuration (the sample-side receive coil cables were connected together, common-mode for this measurement). This common-mode voltage, when connected to both inputs of the P6046, resulted in Curve F. The difference between Curves E and F is the common-mode rejection ratio of the P6046 probe, which was large enough to reduce the common-mode voltage to the sensitivity of the test system.

The linearity of the test system was measured and found to be better than 0.5 dB for MSE ratios of 0 to 60 dB.

The best available indication of the test system's accuracy was that the differences between the theoretical shielding effectiveness of good conductors, such as aluminum and copper, and the measured values of test samples of these materials, were 2 dB. Curve G, as shown in Figure 19, shows this agreement. Long-term repeatability of the test results for a given sample also was good, about 0.5 dB for good conductors and solid laminates, and 1 dB for mesh screens.

The dynamic range for this measurement as seen in Figure 19 can be increased by increasing drive power and increasing receiver sensitivity until system leakage dominates. It is seen to be 80 dB or better above 20 MHz, but declines at lower frequencies. Fortunately, most materials show greater leakage (reduced shielding) at lower frequencies.

5.2 Quadraxial Shielding Test (QUADRAX Facility)

The basic quadraxial test facility has been used to measure the shielding-effectiveness parameters of braided coaxial cables 3 inches or less in diameter. The basic fixture was modified to accept 6-inch diameter cylinders. The modified quadrax is shown schematically in Figure 20.

5.2.1 Quadraxial Test Facility

The quadrax consists of four concentric cylinders. The outer cylinder serves as structural ground and guard shield for the drive line. The drive (signal) cylinder is the next innermost cylinder. At the opposite end of the quadrax the drive cylinder is terminated in 22.8 ohms (eight paralleled 180-ohm, 2-watt carbon resistors). The 22.8-ohm load is the characteristic impedance of the drive cylinder transmission line. The drive cylinder current return is on both the 36-inch-diameter outer cylinder (guard shield) and the sample cylinder. The sample cylinder (6 inches in diameter) is mounted from the rear of the quadrax and is grounded circumferentially to the outer conductor at both ends. The drive end of the sample cylinder was coned down to a 1-inch-diameter cylinder to permit use of a Stoddart 91550-2 current probe to measure the sample skin current, I_s.

The innermost cylinder of the quadrax is the sense rod used to measure the electromagnetic field coupling through the test sample. It is 2.6 inches in diameter so that its characteristic impedance, with respect to the sample cylinder, is 50 ohms. The sense rod is connected to 50-ohm coaxial type N fittings at both ends of the quadrax.

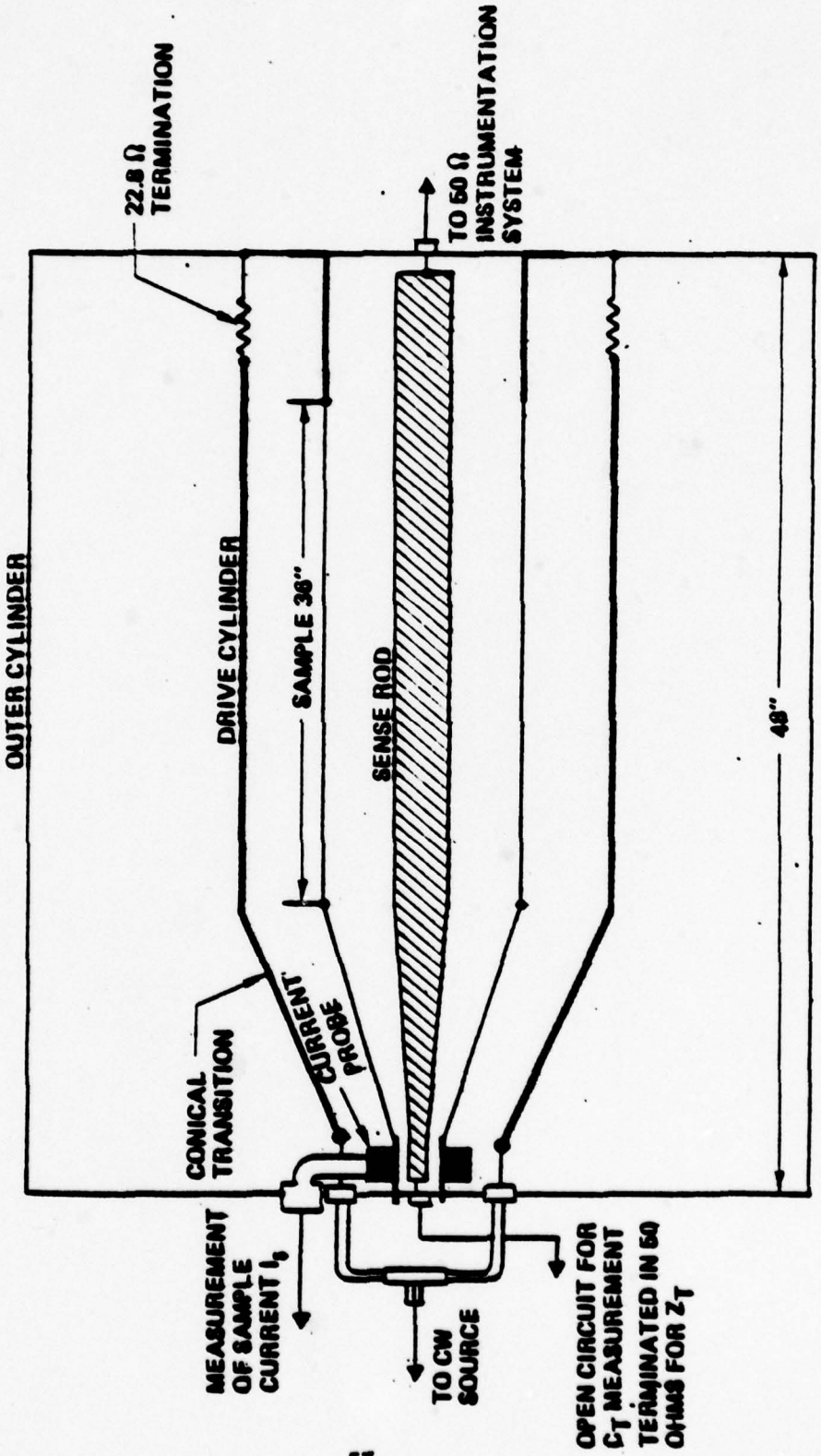

Figure 20: Schematic of Quadraxial Test Fixture

The drive cylinder and the sense rod were both coned down at the drive end of the quadrax to maintain the characteristic impedances of their respective transmission lines.

The sample cylinder and sense rod are installed as a unit. The sample cylinder is clamped to its end plate and conical transition as shown in Figure 21. A photograph of a 40-mil perforated aluminum cylinder installation is shown in Figure 22. The quadrax end plate and sample cylinder aft mounting plate were removed to show the four cylinders.

5.2.2 CW Tests

The quadraxial test facility was used to measure the transfer impedance, Z_T, of composite materials; joint admittance, Y_T, of jointed cylinders; and the transfer capacitance, C_T, through holes in mesh screen. The instrumentation system for the quadrax is shown in Figure 23.

The measurements of Z_T and Y_T were accomplished by measuring the ratio of the sense rod voltage, V_i, to the sample cylinder skin current, I_s. The voltage V_i is measured at the end of the quadrax opposite the drive end, and is equal to the sense rod current, I_i, times the input resistance of the instrumentation system (50 ohms). The drive end of the sense rod also was terminated in 50 ohms. The CW source was direct-coupled to the quadrax drive cylinder which was terminated in its characteristic impedance.

The transfer impedance (Z_T) of the sample in ohms per meter is obtained from the following formula:

$$Z_T = \frac{2V_i}{LI_s} \tag{78}$$

where L is the length of the sample and V_i/I_s is the recorded test data.

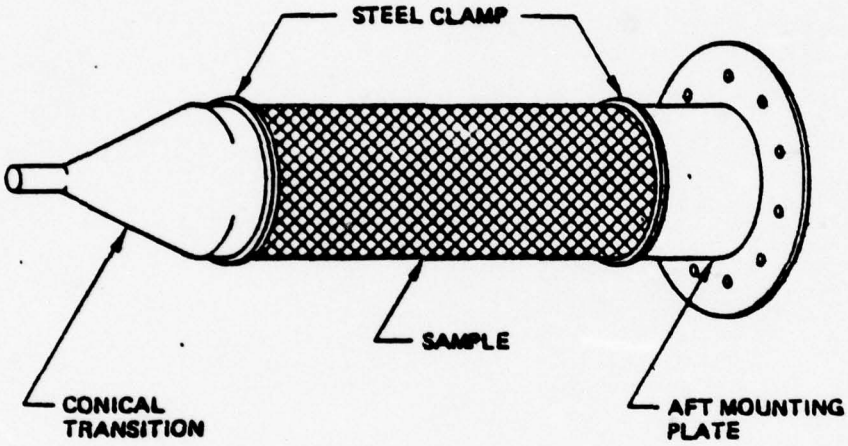

Figure 21: Sample Cylinder Clamping Arrangement

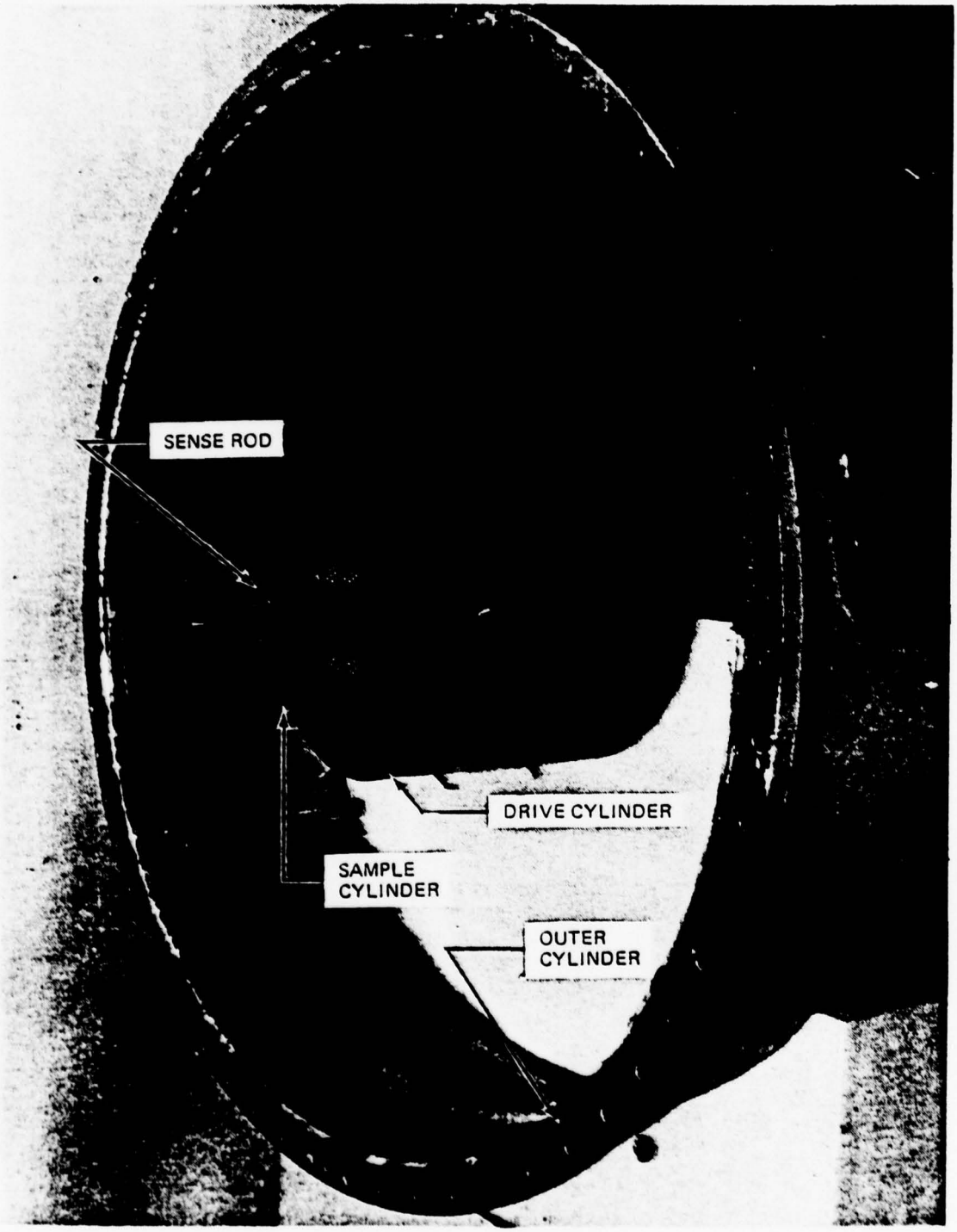

Figure 22: Perforated Aluminum Test Sample in Quadrax

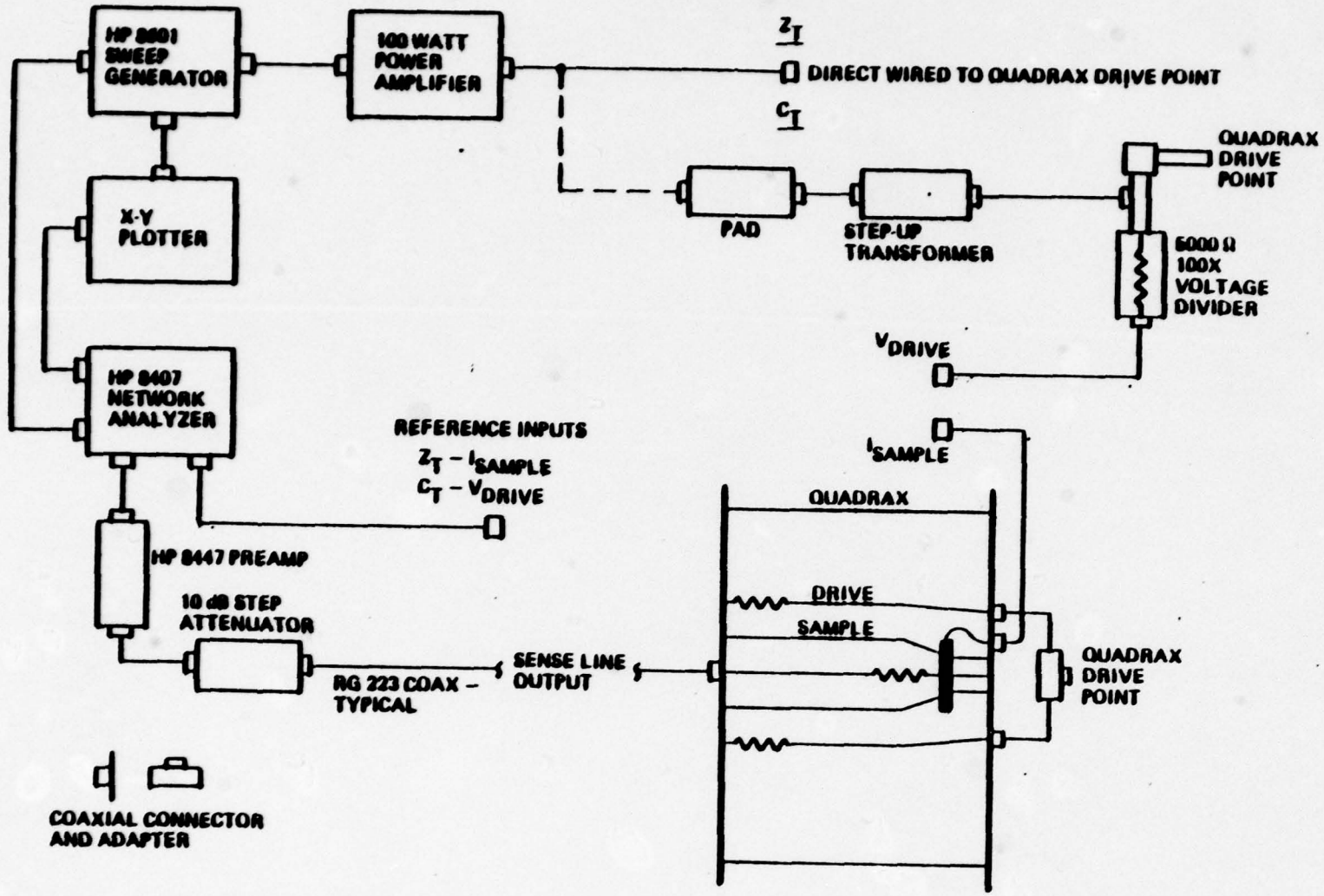

Figure 23: Quadrax – CW Drive and Monitoring Instrumentation

The admittance of a joint was obtained by determining V_i/I_s ratio for an unjointed sample and the jointed sample both equal in length. The following computation then determined the joint admittance per unit width:

$$(2\pi a)^{-1} Y_j^{-1} = Z_j = Z_{js} - Z_T(L-\ell) \tag{79}$$

where

Z_j = Impedance of the joint in ohms
Z_T = Transfer impedance of the unjointed sample in ohms per meter
L = Length of unjointed sample
ℓ = Length of the joint
Z_{js} = The impedance (V_i/I_s) of the jointed sample in ohms
a = Sample radius.

The quadrax test facility was used in what is termed the open-circuit configuration for measurement of transfer capacitance (C_T). The signals of interest for this type of measurement are the sample voltage, V_s, measured at the drive point of the quadrax, and the sense rod voltage, V_i, measured at the end opposite the drive end. The quadrax drive cylinder and the drive end of the sense rod are open-circuited for this measurement. The power amplifier is coupled to the quadrax input via a 3-dB pad (to reduce the VSWR seen by the amplifier) and a step-up transformer (required to improve measurement system dynamic range). As before, V_i, is the voltage measured across the input resistance of the instrumentation system (50 ohms). The sample transfer capacitance, C_TL, may be computed at low frequencies from the test data using the following formula:

$$C_T = \frac{V_i}{(50)2\pi f(V_s)L} \tag{80}$$

where f = frequency in hertz.

The ratio of the desired signals for $Z_T(I_s/V_i)$ and $C_T(V_i/V_s)$ are obtained again using the HP network analyzer system. A preamplifier (HP8447, noise figure 5 dB) was used in the test channel to improve the sensitivity of the V_i measurement. Test results were recorded on the x-y plotter.

Evaluation of the quadraxial test system included the following measurements:

(1) Ambient noise of the instrumentation system and extraneous RF pickup

(2) Z_T of a thin copper cylinder

(3) Measurement of leakage of joints between the sample cylinder and the mounting frame

(4) Repeated measurement of some samples

(5) Input impedance and TDR signature of the drive cylinder and the sense rod.

In the initial fabrication and assembly of the quadraxial test facility, input impedance and time domain reflectometry (TDR) measurements were used to check the drive cylinder and sense rod transmission lines. The impedance of the sense rod does not vary more than ±5 percent, about 50 ohms in the 0.1 to 100 MHz frequency range. The drive cylinder impedance varies between 18 and 30 ohms, and is the prime cause of discrepancies between measurement and theory for mesh cylinders at high frequencies.

Figure 24 shows typical test data obtained in the quadrax. Good agreement between theory and measurement for a 2.7-mil-thick copper cylinder was obtained. Joint leakages for Z_T and C_T measurements were less than -110 and -160 dB respectively. Joint leakage is measured by using a solid, thick sample

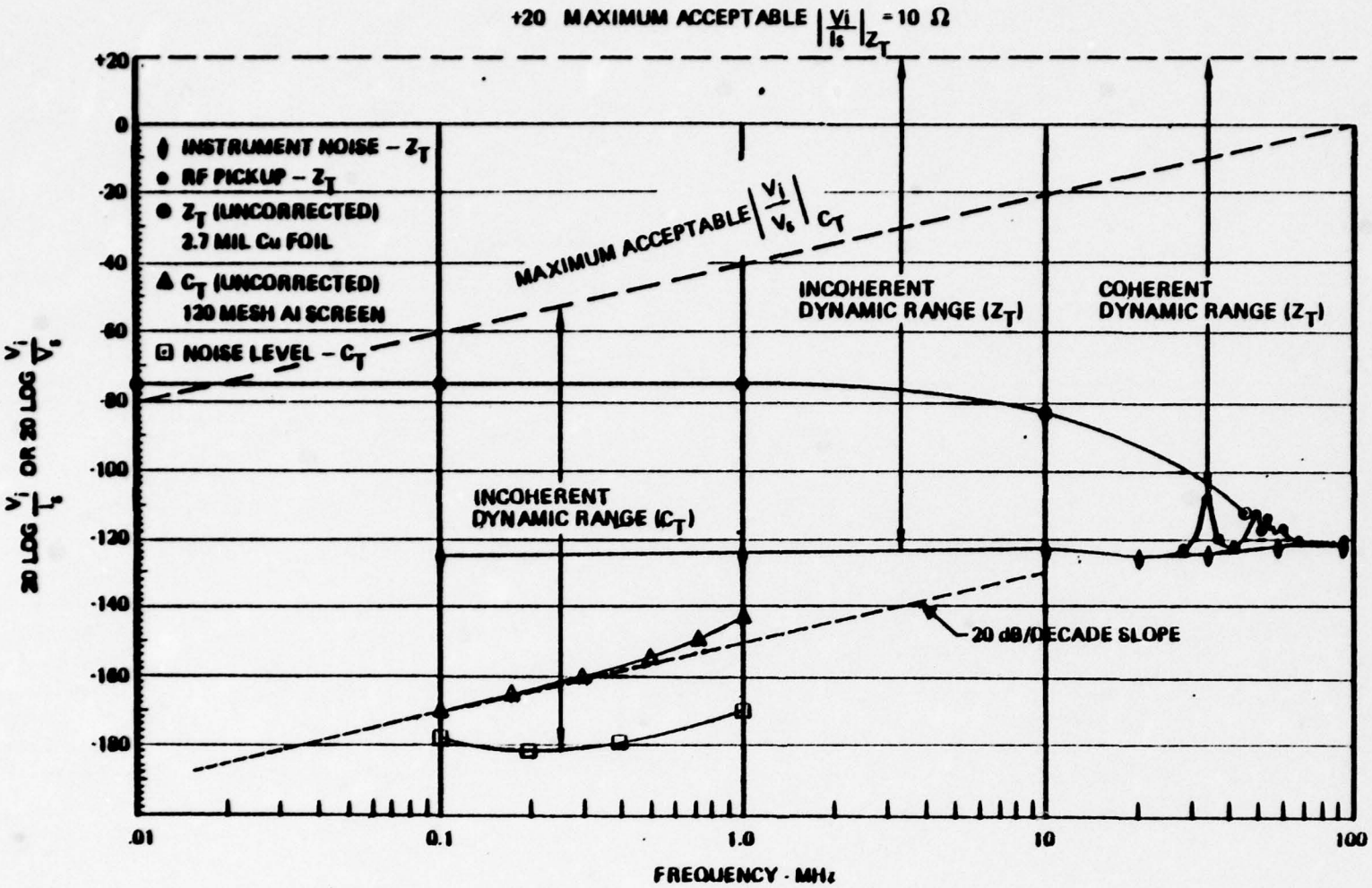

Figure 24: Typical Quadraxial Test Facility Evaluation Data

made from a good conductor. Additional shielding and proper orientation of external cabling was required to reduce RF pickup to a level commensurate with the ambient noise of instrumentation system. Repeatability of measurements was generally 1 dB or better, except some difficulty was experienced measuring fine meshes (C_T). In the use of the quadrax, extreme care is required in installing the sample cylinders so that joint leakage does not affect test data.

The dynamic range for this system is the ratio of the largest Z_T measurable without drive current perturbation;

$$\left|\frac{Z_T L}{2}\right| = \left|\frac{V_i}{I_s}\right| \leq 10 \text{ ohms}; \tag{81}$$

to the smallest Z_T detectable or discernable from system leakage or instrumentation noise (Figure 24). The $\frac{V_i}{I_s} \leq 10$ ohm (+ 20 dB) criterion limits drive perturbation to about 1 dB. If the coherent noise floor (leakage) is exceeded by 6 dB the largest error possible (due cancellation effects) is 6 dB. Exceeding the incoherent "receiver" instrumentation noise by 6 dB results in less than 6 dB error. The dynamic range is seen in Figure 24 to exceed 140 dB for 0-30 MHz. This incoherent dynamic range can be increased by increasing drive power and lowering receiver noise figure until the limiting coherent dynamic range is reached. Above 30 MHz, leakage dominates and the dynamic range exceeds 130 dB, approximately.

Similarly, for the C_T measurement, C_T should not be large enough to load the 50 Ω drive system substantially at the high frequency limit. So that

$$\left|\frac{V_i}{V_s}\right| = 25\, W_{max}\, C_T L \leq 1, \text{ or} \tag{82}$$

limits the loading error to 1 dB and sets the upper limit of acceptable $\frac{V_i}{V_s}$ at 0 dB in Figure 24. The incoherent dynamic range for C_T is seen to be frequency dependent increasing with frequency to 1 MHz where it is about 130 dB. Above 1 MHz becomes roughly constant and should exceed 120 dB up to 100 MHz.

5.3 The Anechoic Chamber

The anechoic chamber measurement system is shown in Figures 25 through 27. This system has been described in detail in reference 9. RF isolation is achieved by placing a transmit antenna inside an anechoic chamber with the test specimen electrically connected to one end of the chamber by means of a special holder. Initial measurements showed that leakage around the periphery of the specimen could easily exceed the transmission through the specimen and therefore invalidate the data. The leakage was greatly reduced by using the improved sample holder shown in Figure 27, sanding the specimen around its periphery to achieve good electrical contact to the holder and by applying conductive adhesive copper tape around the holder-to-sample interface.

Despite these efforts, RF leakage still masked or distorted the data. To minimize RF leakage effects, it was necessary to place the receiver horn directly on the test specimen and apply copper tape around the horn periphery. Then Emerson Cuming (AN 75) microwave absorber material was placed around the horn as shown in Figure 26. These techniques reduced the leakage paths sufficiently to acquire loss data, although, as will be seen in the following section, some leakage apparently still occurs at the higher microwave frequencies.

A measurement error is introduced into the system due to the techniques used to reduce leakage into the receiver. The antenna aperture fields are distorted when the antenna is placed directly onto the test specimen. Although field probing of the chamber aperture, without specimen, showed a reasonably uniform (± 2 dB) electric field, introduction of the test specimen and the absorber covering the specimen did result in field distortion.

Recommendations for improving the free space measurement system are given in reference 9. Among the most important of these recommendations is the technique for improving the electrical connection between the test specimen and the sample holder, thereby minimizing RF leakage. If the RF leakage can be reduced sufficiently to place the receive antenna several antenna apertures away from the test specimen, eliminating the absorber material from the specimen, the measurement error would be reduced.

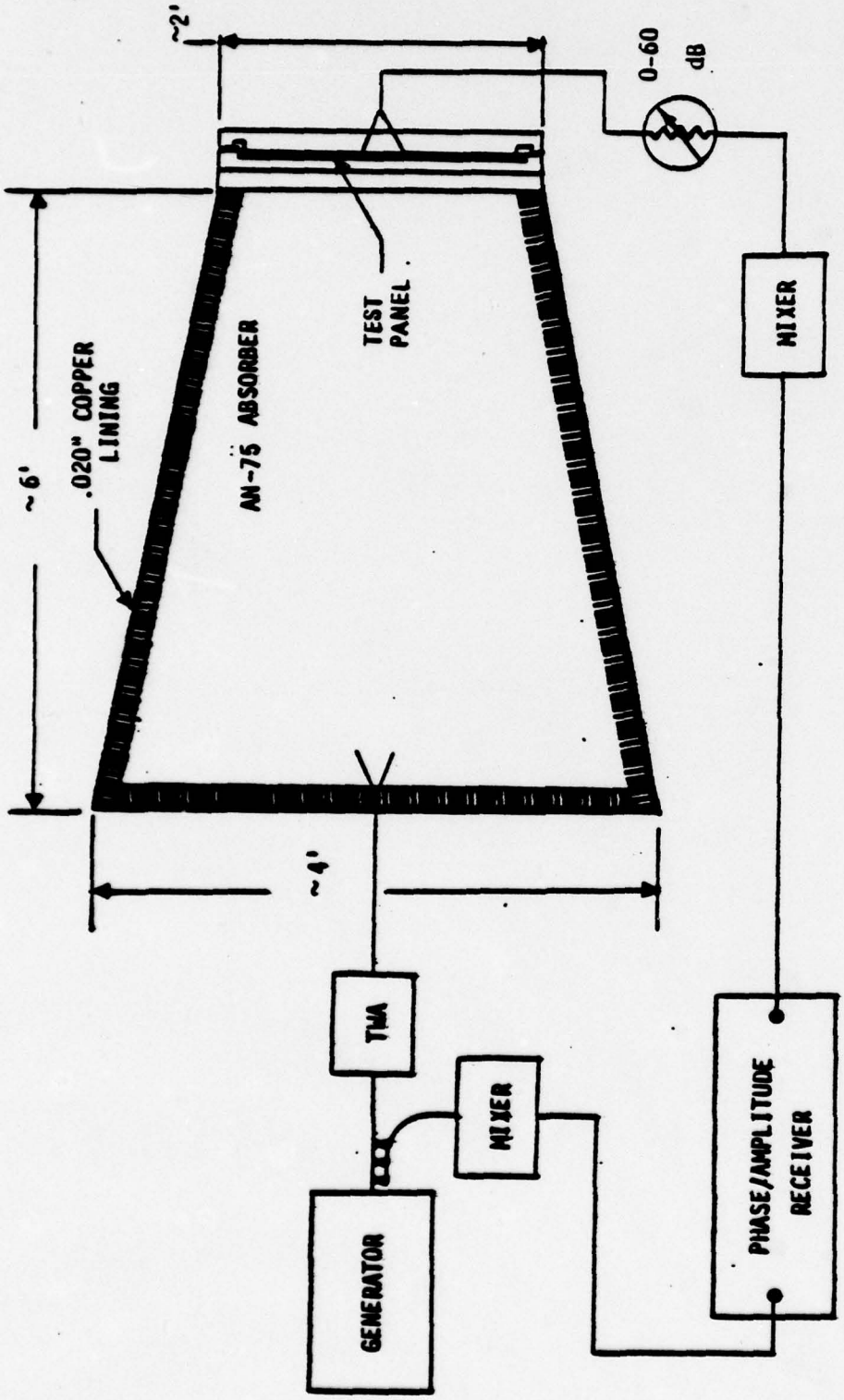

Figure 25: Freespace Transmission Test System

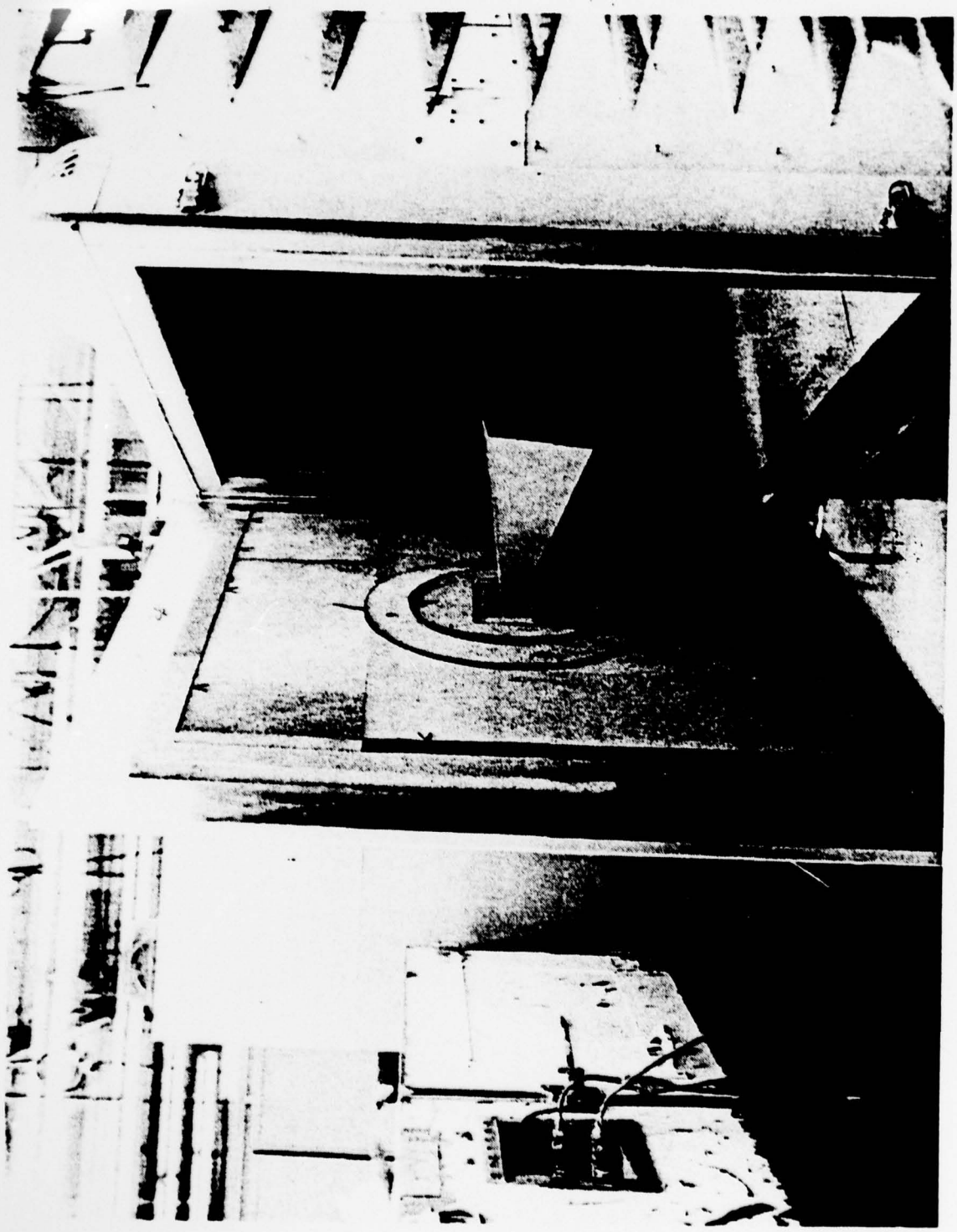

Figure 26: Anechoic Chamber – Transmitter

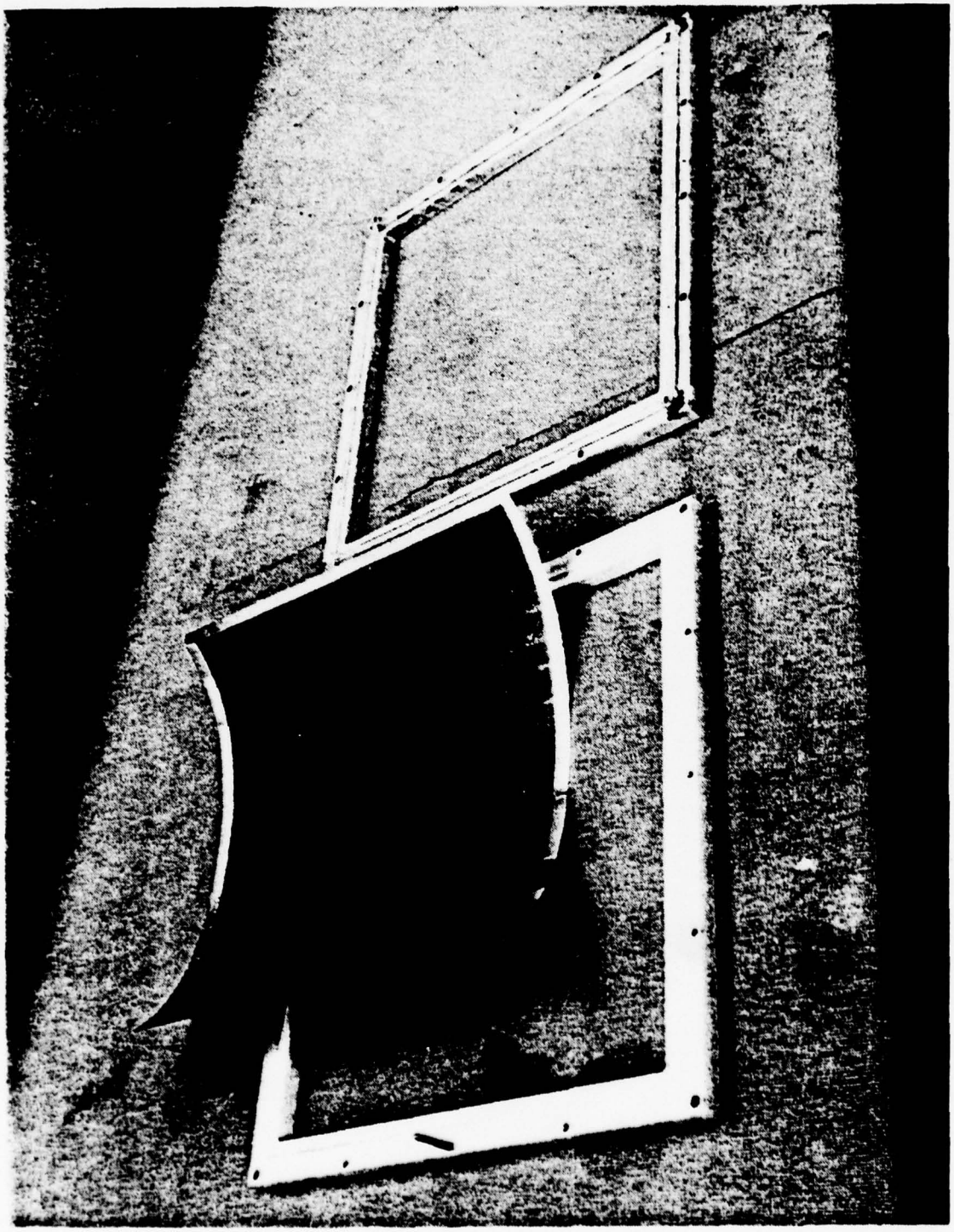

Figure 27: Sample Holder — Dissambled

The estimated uncertainty due to calibration errors, receiver nonlinearity, transmit antenna to test specimen interaction, power drift, receiver signal-to-noise ratio, and RF leakage are estimated to be 5% (dB) of the transmission loss. This estimate is based upon known accuracies of the equipment and the reproducibility of the data. Many of the error sources are frequency and test geometry (e.g., antenna aperture size and placement) dependent. These uncertainty estimates are included in the data shown in the following section.

Free space transmissivities of four ply cross ply [0, ± 45, 90] degree laminates were measured over the frequency range from 1 to 18 GHz. The material used was Hercules AS 3501-6B with a thickness of approximately 0.005 in. per ply. Using the computational technique of reference 9, the bulk conductivity was computed as a function of frequency.

Figures 28 through 31 are representative of the measured four ply composite data. Curve (1) is the reference data without the specimen. The variations in the magnitude are due to:

(1) Generator power fluctuations as a function of frequency

(2) Mixer response as a function of frequency

(3) Variations in receiver gain as a function of frequency

(4) Variations in chamber reflection characteristics as a function of frequency

(5) Area of specimen measured differs as function of antenna used.

Each set of data represents the maximum frequency range that could be swept due to required changes of generators, mixers, antennas, traveling wave-tubes (TWT), or combinations of these, primarily due to their limited frequency bandwidth. Each of the reference curves is labeled with a value referencing a

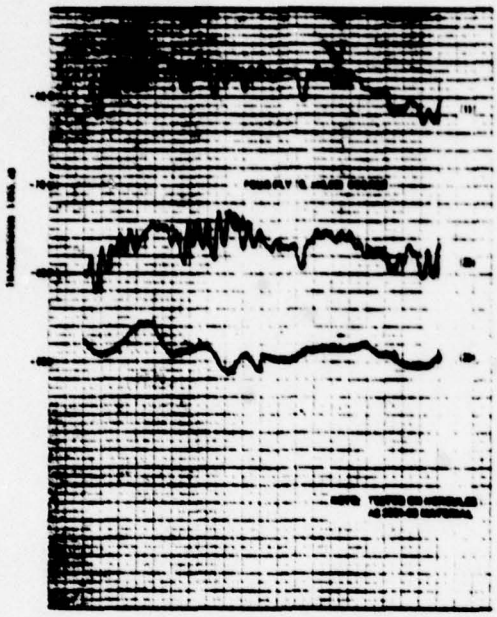

Figure 28: Four-Ply Transmission Data, 1.0 to 1.7 GHz

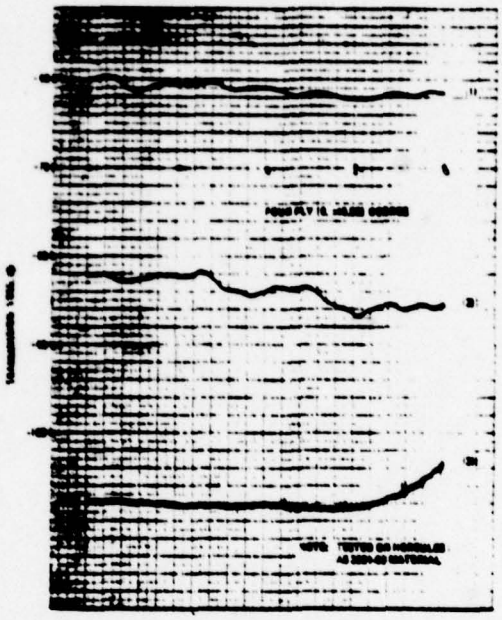

Figure 29: Four-Ply Transmission Data, 1.7 to 2.0 GHz

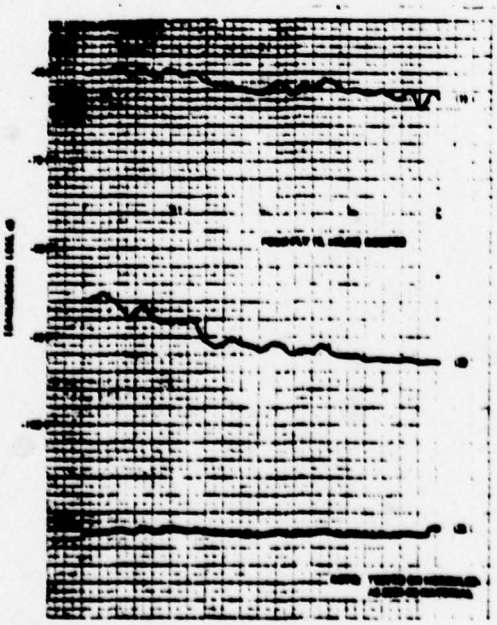

Figure 30: Four-Ply Transmission Data, 2.0 to 2.6 GHz

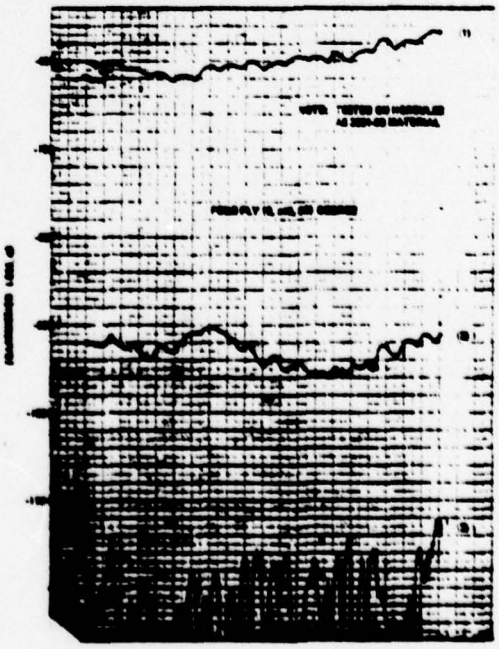

Figure 31: Four-Ply Transmission Data, 2.6 to 3.0 GHz

series attenuator; the attenuation was required because of the limited dynamic range (≈ 60 dB) of the receiver system. When the test specimen was installed, the attenuator was removed, thus providing a technique for achieving the dynamic range required without changing the gain of the receiver system. The transmission loss with the specimen removed is 60 dB less than indicated in the figures.

Curve (2) is the measured loss with test specimen installed. Fluctuations in these data are due to the equipment responses and variations as listed above. Other variations are due to interference between leakage energy summing with the transmitted energy and receiver noise contained in the signal.

Curve (3) is the measured receiver system noise level when the test specimen was replaced by an aluminum plate. Variations in this noise level are primarily due to variations of receiver sensitivity with frequency and cross talk between the reference and test channels. The measured noise level with a 50-ohm load was similar to that of the aluminum plate. The transmitted signal was masked by the noise for frequencies from 12 to 18 GHz. Therefore, the data is not presented here. The noise level was on the order of -125 dB in the 12 to 18 GHz range, therefore a lower bound value of conductivity can be calculated.

These lower bound conductivity values are included in reference 9 and Figure 32. Concrete values of shielding and conductivity would be more desirable, however. It was estimated that at least 20 dB more signal power or increased receiver sensitivity would be required to achieve adequate signal-to-noise ratio for quantitative data. The receiver sensitivity is on the order of -100 dBm at 18 GHz; this is about the limit for any broadband receiver. The microwave amplifier power output is 10 watts; a 1000-watt source would be required to achieve a 20 dB increase in signal-to-noise ratio. A 1000-watt source was not available at K_u band (even if it were, other problems might accrue, such as microwave heating of the anechoic chamber absorber material). Therefore, attempts to measure the absolute loss of graphite/epoxy four-ply symmetrical laminates above X-band were not feasible using the anechoic chamber measurement technique.

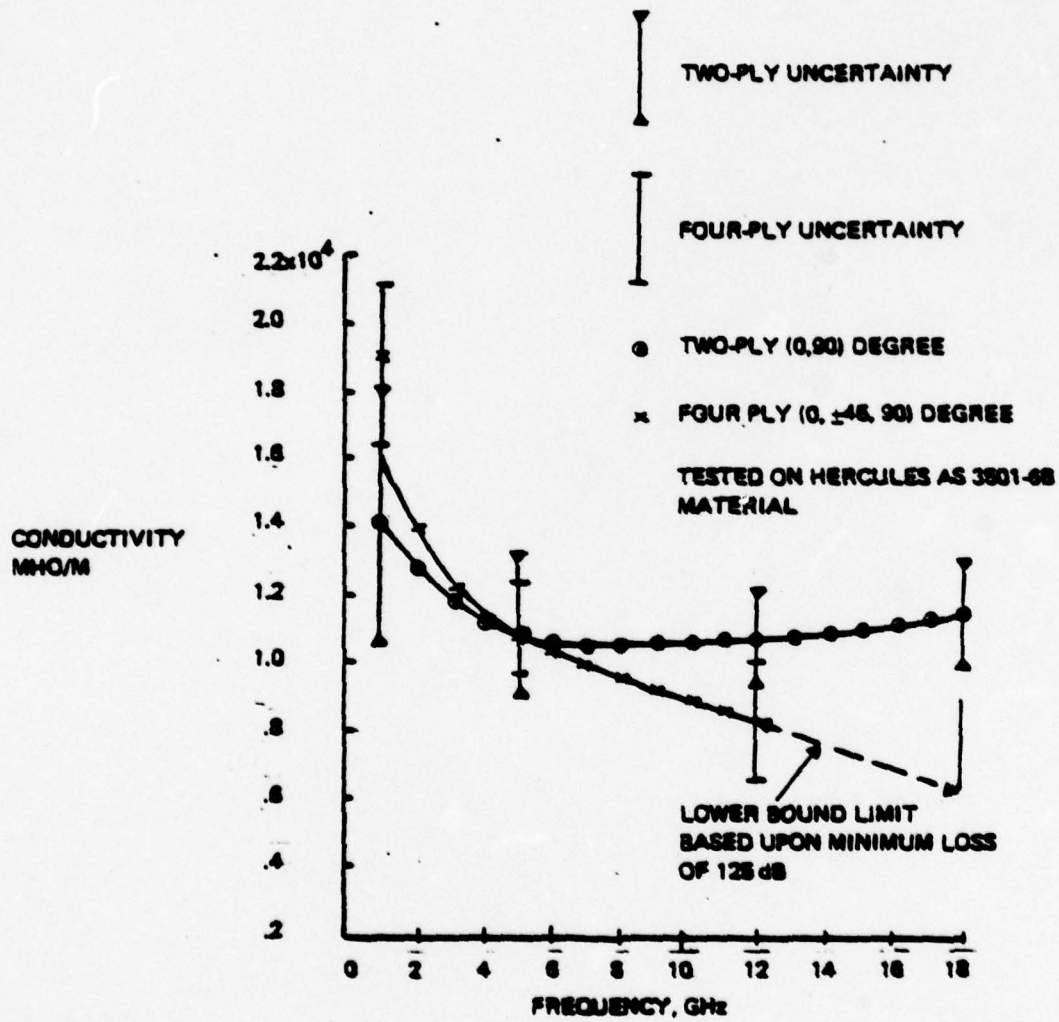

Figure 32: Conductivity Versus Frequency

An alternative to achieving a greater signal-to-noise ratio is to measure a thinner material such as a two-ply [0, 90] degree laminate. Disadvantages to measuring a two-ply laminate are:

(1) The laminate is so thin that small deviations in thickness can lead to large deviations in measured loss.

(2) Small imperfections in the lay-up may cause significant differences in measured loss.

(3) The lay-up, although symmetrical, is not typical nor does it correspond physically to the four-ply lay-up.

The losses were predicted to be on the order of 30 dB less than the four-ply laminate, thus significantly improving the signal-to-noise ratio. Further, even through the calculated conductivity of the two-ply laminate might differ from the conductivity of the four-ply laminate, if the trends were similar, the confidence in the data would be improved. Thus, a two-ply laminate was fabricated and measured.

Conductivity values differ somewhat for the two and four-ply laminates. There are uncertainties in the loss data due to differences in lay-up as well as uncertainties attributable to the measurement system. Because the four-ply laminate is more representative of a typical structural lay-up, the four-ply data are recommended for computing the loss in symmetrical panels. Since the data above 12 GHz was calculated using the receiver noise threshold, which yields a 125 dB loss, it represents a lower bound on the conductivity; that is, material losses will always be greater than the lower bound would indicate. Therefore, when data above 12 GHz are required, the four-ply lower bound conductivity value, as shown in Figure 32, will provide a conservative loss estimate.

The four-ply data from 5.0 through 12.4 GHz contains considerable noise. Thus, over that frequency range the mean value between maximum and

minimum signal was calculated and those values were plotted. Finally, a linear regression was performed over each frequency range to smooth the data even more. Smoothing the data in this manner considerably aided the computation of conductivity shown in Figure 32. RF conductivity was calculated from the measured loss data (see reference 9). These data include the possible error due to measurement uncertainty.

The plane wave shielding effectiveness of graphite/epoxy laminates (at microwave frequencies) has been found to be very high, although not as effective as aluminum. Graphite/epoxy laminates should provide substantial shielding. A more significant problem is the characterization of RF leakage through structural joints, composite to composite or composite to metal. Unless excellent electrical connectivity exists across a joint, RF leakage will exceed direct diffusion through the material. Providing good electrical contact with graphite composite is very difficult because contact with the graphite fibers must be obtained. Some techniques utilizing wire screen are examined in reference 1 and exemplified in Figure 33.

The anechoic chamber transmission test technique performed adequately for frequencies up to 12 GHz (four-ply laminates) and 18 GHz (two-ply laminates). Higher transmit power (> 1000 W) and/or greater receiver sensitivity (< -120 dBm) would be required to measure the four-ply composite properties above 12 GHz. Because of potential microwave heating of the chamber absorber lining, the preferred technique would be to use a more sensitive receiver or a pulsed system. The greatest source of measurement error was due to RF leakage around the periphery of the specimen. Figure 33 illustrates a specimen fabrication technique that would minimize this leakage. The wire screen would be co-cured with the composite material thus providing good electrical connectivity. Removal of excess resin from the screen on the outside surface would be required.

This system required ten separate frequency runs to cover 1-12.4 GHz owing to the band limitations on the horns, sources, and receivers involved. Extension to 18 GHz would add two to three more ranges. This situation threatens

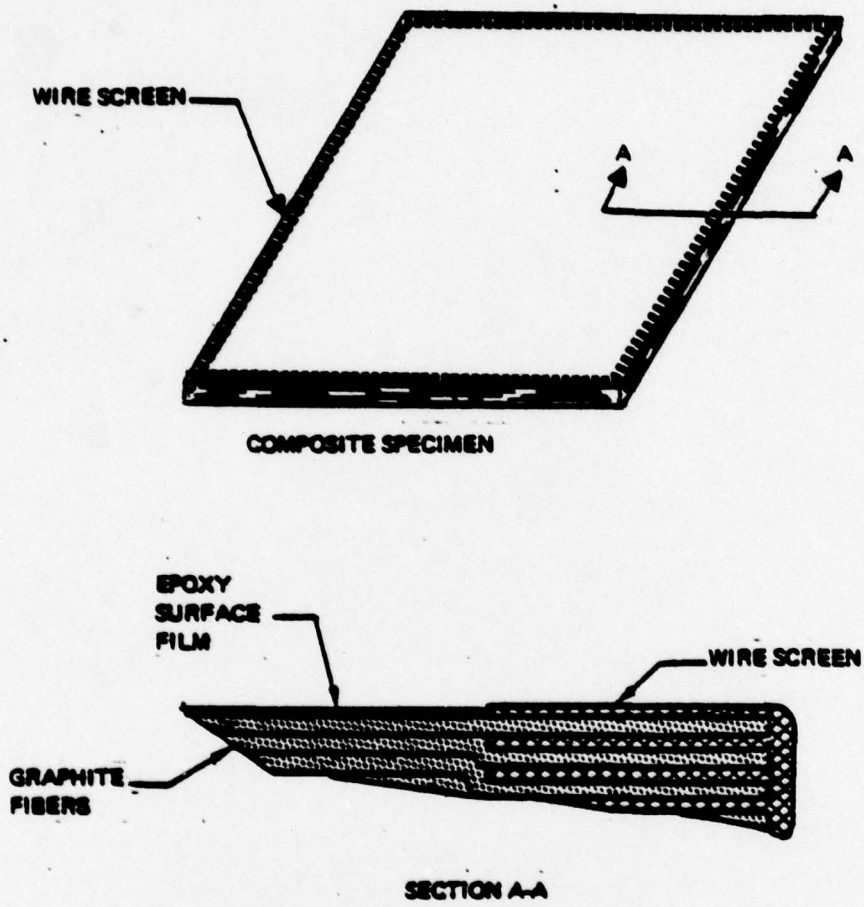

Figure 33: Test Specimen Edge Treatment Concept

to slow the measurement scheme to perhaps one or two samples per measurement day. This would be approximately an order of the magnitude slower than the familiar HF parameter measurement schemes (stripline, FPT, etc.). At the present time, available test equipment would seem to be limited to swept measurements in octave bandwidths below 4 GHz and manual measurements in octave or sub-octave bandwidths above 4 GHz. Log periodic or other broadband antennas might cover the desired range with as few as perhaps one or two antennas. A hybrid antenna covering 1-18 GHz with multiple feeds requiring only external coax switching may be feasible.

6.0 REVIEW OF INSTRUMENTATION SYSTEMS USED TO MEASURE MICROWAVE LEAKAGE THROUGH PANELS

Block diagrams of two major systems used to measure leakage through panels[9] in the 1-18 GHz frequency range are shown in Figures 25 and 34.

In Figure 34, an HP 8410/8411 network analyzer system is the main component. The main advantage of the HP 8410/8411 is that it is reliable (repeatable) and can be swept over the entire range of frequencies (.1-12.4 GHz HP 8410/8411 A; .1-18 GHz HP 8410 B/8411 OPT 18) in one step. Its main disadvantage is the poor sensitivity (-78 dBm with 10 kHz BW) and limited operating range for the reference signal ($\leq$ 6-10 dB variation in level).

In Figure 25, the Scientific Atlanta Model 1750 phaselocked receiver is the primary component. Its main advantage is its sensitivity (better than -105 dBm with 1 kHz BW). The main disadvantage of the Model 1750 is that it cannot sweep the entire band (2-18 GHz) in one step. Its phaselock system apparently is partially mechanical and therefore very slow. A second disadvantage of the Model 1750 is that it requires external mixers above 2 GHz.

The remaining parts of the instrumentation include directional couplers, attenuators, coaxial cables, sweep oscillators, TWT (power) amplifiers, antennas, and an anechoic chamber which are common to Figures 25 and 34. The couplers, attenuators, and cables are broadband devices. The sweep oscillators, TWTs, and antennas limit measurement productivity. Typically the oscillators and TWTs must be changed in each of the following bands:

$$\left.\begin{array}{r} .2 - 2 \\ 2 - 4 \\ 4 - 8 \\ 8 - 12 \\ 12 - 18 \end{array}\right\} \text{GHz}$$

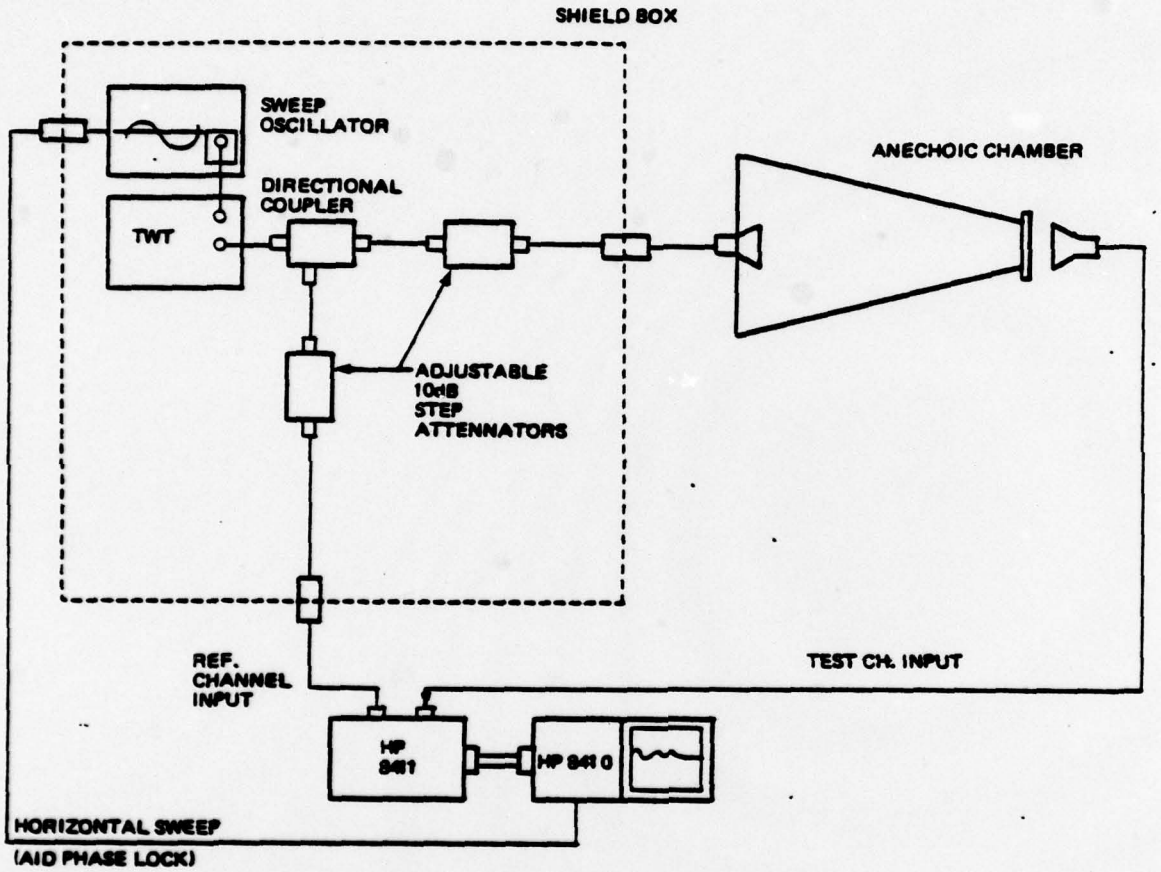

Figure 34: Microwave Measurement System

The antennas consisted of a set of standard gain horns which also limited productivity and were changed for the following frequency bands:

$$\left.\begin{array}{l} 1.0 - 1.7 \\ 1.7 - 2.6 \\ 2.6 - 3.95 \\ 3.95 - 5.85 \\ 5.3 - 8.2 \\ 8 - 12.4 \\ 12.4 - 18 \end{array}\right\} \text{GHz}$$

Admittedly, the number of antennas used over the 1-18 GHz range can be reduced to the 5 ranges required by the sweep oscillators and TWT amplifiers.

The anechoic chamber limited the dynamic range available for measurement due to leakage in joints made of copper tape and between the sample panel and its mounting hardware. Much copper tape was used in previous tests to reduce coherent noise below the data of interest. In general, coherent noise was reduced to the random noise level sensitivity of the HP 8410/8411 for a 10 watt TWT, but not that of the Scientific Atlanta Model 1750.

6.1 Anechoic Chamber: Preliminary Evaluation

The setup shown in Figure 34 has been evaluated for the 3-4 and 8-12 GHz frequency bands using a 1 watt TWT amplifier. Several panels made of 3 mil aluminum foil were fabricated. One panel had a row of 1/16" diameter holes spaced 1/4" apart. A second panel had a row of 1/10" long thin slots with 1/5" spacing between the ends of each slot. A third panel had a row of large slots, 1/4" (wide) 1/16" (gap) spaced at 1/2" intervals (centers of the slots). A fourth panel had no apertures and was used to measure noise.

Test results indicated the following:

1. Dynamic range of 80 dB 3-4 GHz (noise floor
   60 dB 8-10 GHz corresponds
   50 dB 10-12 GHz to -75 to -78 dBm)

2. Copper tape is required to reduce coherent noise in the 3-4 GHz band.

3. Very low signal-to-noise ratios were obtained for the panel with a line of small holes or thin slits ($S+N|N \leq 10$ dB)

4. Projected test time for the 1-18 GHz frequency band would be about 16 hours per test panel.

5. The sensitivity of the HP 8410/8411 is commensurate with the coherent leakage in the anechoic chamber with a TWT amplifier of rated power of 1 to 10 watts.

6.2 Preliminary Conclusions

In order to improve the productivity, dynamic range, and reliability of leakage measurements at microwave frequencies the following steps/improvements are required:

1. Improve the sensitivity of the HP 8410/8411 by adding low noise microwave FET amplifiers to the HP 8411A Test Channel Input. Improving the selectivity and gain of the HP 8410A second IF circuitry. Off-the-shelf preamps with gains of 30 dB and 8 dB noise figure are available in the 2-8 GHz and 8-18 GHz bands. The IF circuitry in the HP 8410 is similar to that in the HP 8407 Network Analyzer which has previously been improved by Boeing under a DNA contract. The estimated improvement was 30 dB.

2. Reduce leakage in the anechoic chamber by 40 dB or more.

3. Develop antennas to cover the frequency ranges consistent with the preamps (2-8, 8-18 GHz).

4. Obtain state-of-the-art sweepers which can cover <2 to 18 GHz in one or two sweep ranges. These are available from Willtron and Hewlett Packard.

5. Use multiport coaxial switches and stack TWTs (> 10 watts) so that the equipment changes can be limited.

These improvements will still require the frequency range to be broken into 5 bands, but no equipment changes would be required. Estimated test time per panel, including mounting, would be approximately 1 hour assuming equipment startup calibration/checkout procedures, (1.5 hours), are complete.

7.0 SUMMARY

The measurement schemes studied in detail were limited to those previously used for measurements of this type and which employ flat plate samples. Flat plate samples are relatively easy to fabricate and install.

The exception to this rule is the Quadrax facility. It uses cylindrical samples which are costly and difficult to install, but it has the greatest sensitivity (dynamic range) of any system considered. It has been used on several programs for material parameter and joint measurement as well as cable braid measurement. It is easily analyzed, provides very good accuracy, and can be used as a standard of comparison for other techniques.

The "standard" Quadrax, the magnetic flat plate test facility, the stripline test facility, and the anechoic chamber were evaluated for material parameter z_s and joint admittance Y_J measurement. The first three have been used through the VHF region; the fourth has been used at UHF and microwave frequencies. They are all capable of both types of measurements (z_s and Y_J) and are all extendable to greater frequency range.

Each of the above have been evaluated from the point of view of frequency range, sensitivity (and dynamic range), measurement accuracy, and measurement times. These necessarily involve a heuristic approach in the frequency range beyond their previous application. A tabulation of the estimated performance characteristics of these measurement facilities is given in Table I.

<u>Current Frequency Range</u> refers to that range with previous documented experience where performance characteristics are well known. The useful frequency range depends upon the availability of RF sources and receivers, network analyzers, spectrum analyzers and sweepers, etc. as well as upon

Table I. Estimated Performance

Facility	Current Frequency Range	Probable Frequency Extension	Parameter Sensitivity Y_J (℧/m)	Parameter Sensitivity Z_S (Ω)	Dynamic Range	Estimated Measurement Time	Estimated Measurement Accuracy
Quadrax	.001-100 MHz	1000 MHz	4×10^5	2×10^{-6}	130 dB	2 Samples/Day	2 dB (6 dB)
FPT	.001-100 MHz	300 MHz	$\frac{4\times10^4}{\left\lvert 1+j\frac{f_m}{20}\right\rvert}$	$4\times10^{-4}\left\lvert 1+j\frac{f_m}{20}\right\rvert$	70 dB	12 Samples/Day	3 dB (6 dB)
Stripline	.001-100 MHz	1000 MHz	$\frac{3\times10^4}{\left\lvert 1+j\frac{f_m}{25}\right\rvert}$	$7\times10^{-5}\left\lvert 1+j\frac{f_m}{25}\right\rvert$	95 dB	6 Samples/Day	3 dB (6 dB)
Anechoic*	1-18 GHz	-----	300	2×10^{-2}	80 dB	6 Samples/Day	6-10 dB

* Tentative: Reflects current performance near 3-4 GHz — Leakage limited at present.

facility response. Automatic swept frequency - coherent detection equipment is available from 1 kHz to 2 GHz with three sets of gear (1-100 kHz, 0.1-100 MHz, and 0.1-2 GHz). Above 2 GHz, manual tuning of source and receiver or spectrum analyzer is the rule although automated measurement schemes are becoming available at fairly high cost. Measurement accuracy generally declines above 100 MHz.

Probable Frequency Extension refers to the expected achievable upper frequency limit of the gear in question when steps are taken to reduce leakage around the sample and multimoding field nonuniformities and resonances and when receiver sensitivity and source power level are increased to the limit of available commercial equipment. It should be noted that dimensional changes aimed at raising the upper frequency limit will generally reduce system sensitivity at the lower frequency limit.

Parameter Sensitivity is the limiting values of Y_J and z_s that can be accurately discerned from receiver noise and facility leakage (coherent noise) over the current range. In general, sensitivity declines as the frequency range is extended.

Dynamic Range is a commonly used but ambiguous term which relates the largest measurable sample leakage (z_s), without excessive error due to field distortion, reference saturation, or equipment overload, to the minimum detectable sample leakage without excessive error due to receiver or coherent noise. When substantial source power (watts or tens of watts) is used the lower limit is normally set by coherent noise not receiver noise. The upper limit is normally set by field distortion. Coherent noise is set by the overall shielding quality of the facility. The [illegible] leakage sources involved are very difficult to estimate analytically although they are commonly inductive in character (increasing as ω). This leakage is normally reduced experimentally to the lowest achievable within allowed time and budget and is empirically determined. If the sensitivity limit is set by the receiver (noise), as it is for low power sources, the sensitivity and dynamic range are calculable analytically.

Estimated Measurement Time is described in terms of the number of planar samples which can be measured per day in the "current frequency range" for either z_s or Y_J. The numbers should be considered as near optimum numbers obtainable by experienced personnel, with sufficient time allowed for twice daily equipment calibration and sufficient care to achieve the stated accuracy. Measurement time increases with the number of frequency bands (equipment sets) that must be connected and calibrated per sample run. The indicated frequency extensions will roughly double the measurement time per sample (half the given numbers in the table).

Estimated Measurement Accuracy should be interpretted as the +/- dB error limit of the system with carefully calibrated equipment in the "current frequency range." The figures in the parentheses are anticipated attainable error limits in the extended frequency range.

8.0 RECOMMENDATIONS

Owing to a general lack of information on joint and material parameters above 100 MHz, it is recommended that work start in this area. Extension of the frequency range of the previously developed (< 100 MHz) systems, such as the stripline or FPT, as far into the 100-1000 MHz range as possible, is one possibility.

Unless there now exists a pressing need for data in this latter range, it is recommended that the 1-18 GHz range be approached first. This means, essentially, the development of a high quality anechoic chamber with internal broadband excitation and pickup antennas. This development effort should include:

a. Development of a low leakage chamber which facilitates sample mounting while maintaining leakage near or below the best available receiver sensitivities (2-5 dB noise figure, 1-10 kHz BW coherent detection, and 10 watts power input).

b. Development of wide band antennas (probably LPDA) to cover the intended frequency range without remounting of antennas. Multiple antennas should be fixed mounted with coaxial feeds brought out so that time consuming entry into the chamber is necessary only to change samples.

c. Instrumentation systems must be designed and arrayed to facilitate band changing of equipment within the 1-18 GHz range.

As indicated in earlier sections, the measurement effort will be slowed greatly if the normally available hand swept equipment is used to cover the upper portion of the design frequency range. The Navy can help in

this development effort by providing measurement equipment (ultimately to be used with the delivered anechoic chamber) to Boeing for use during the development phase of the contract.

Following the development phase, Boeing constructed and government supplied jointed panels should be measured as planned.

REFERENCES

1. Strawe, D. and Piszker, L., "Interactions of Advanced Composites with Electromagnetic Pulse (EMP) Environment," AFML-TR-75-141, The Boeing Company, September 1975.

2. Schelkunoff, S. A., Electromagnetic Waves, D. Van Nostrand Co., New York, 1943.

3. Kaden, H., "Wirbelstrome Und Schirmung in der Nachrichtentechnik," Springer-Verlag, Berlin, 1959.

4. Vance, E. F., and Chang, H., "Shielding Effectiveness of Braided Wire Shields," SRI Technical Memorandum 16, November 1971.

5. Bethe, H. A., "Theory of Diffraction by Small Holes," Phy. Rev. 60, pp. 163-182, 1942.

6. Marcuvitz, N., Waveguide Handbook, MIT Rad. Lab. Series, Vol. 10, McGraw Hill, New York, 1951.

7. Bouwkamp, C. J., "Diffraction Theory," Philips Res. Rep., No. 5, pp. 401-442, Dec. 1950.

8. Collin, R. E., Field Theory of Guided Waves, New York: McGraw-Hill, 1960, p. 68.

9. Force, R. D., et al, "Investigation of Electromagnetic Energy Effects on Advanced Composite Structures and Their Associated Avionics/Electrical Equipment," Phase II, Vol. 1, Technical Report, D180-20186-4, Sept. 1977.

10. Whitson, A. L., and E. F. Vance, "Bolted Lapped-Joint EMP Shields," DNA Technical Report DNA 4472F, SRI International, June 1977.